Analysis of deuteron evaporation from ^{64}Ge*, ^{56}Ni*, and ^{52}Fe*

Author:
Seán McCaughley

Supervisors:
Dirk Rudolph
Yuliia Hrabar

LUND UNIVERSITY

May 2024

Abstract

This paper analyses deuteron evaporation in comparison to the evaporation of a proton-neutron pair for different compound nuclei. The main reaction is the fusion-evaporation reaction of ^{40}Ca on ^{24}Mg target leading to the formation of the ^{64}Ge* compound nucleus, along with other contamination reactions. The experimental dataset is obtained from Argonne National Laboratory. Projections on γ-γ matrices were used to analyse the γ-ray spectra of ^{61}Zn, ^{58}Cu, ^{53}Fe, and ^{49}Cr. The results suggest that the relative rate of deuteron evaporation compared to a proton-and-neutron evaporation has a dependence on spin and excitation energy for the dp and 2pn evaporation channel. The rate of deuteron evaporation may also have a mass number dependence.

Acknowledgments

I would like to give my most sincere gratitude to my supervisor Dirk Rudolph for the advice and support I received throughout the thesis. I give my thanks to Dirk for introducing me to the field of nuclear physics along with giving me the opportunity to work on an exciting project. Dirk provided detailed feedback to many draft thesis's along with guidance on more theoretical aspects of the thesis. The guidance has improved me as a writer and aspiring physicist.

I give my sincere gratitude and thanks to my co-supervisor Yuliia Hrabar. The countless hours of guidance ranging from coding, to advice on the thesis has been instrumental in creating this project. Without her advice and help with ROOT and other aspects of the project, the project wouldn't have completed. I thank her and Dirk for analysing and helping me interpret the results of the thesis.

Finally, I would like to acknowledge the help my family has provided me. To my mam, dad, brother, uncles, aunts and cousins without your support throughout my project, studies and life I would not have had the opportunity to study at Lund and to write this thesis.

Contents

List of Acronyms

- **ANL** - Argonne National Laboratory
- **DSSD** - Double-Sided Si-strip Detector
- **ATLAS** - Argonne Tandem Linac Accelerator System
- **2pn** - two protons and one neutron
- **dp** - deuteron and proton
- α**pn** - α particle, proton and neutron
- α**d** - α particle and deuteron
- **FMA** - Fragment Mass Analyser
- **BGO** - Bismuth Germanate Oxide
- **HPGe** - High-Purity Germanium
- **CsI(Tl)** - Caesium-Iodide Thallium doped

1 Introduction

In 1911 it was discovered by Ernest Rutherford that a nucleus is at the core of every atom along with experimental confirmation of the proton. Already twelve years before, in 1899, the α particle was experimentally found as a decay process of uranium by the same Rutherford. In May of 1932 the neutron was discovered by James Chadwick. With both the proton and neutron experimentally confirmed the modern picture of a nucleus composing of a number of protons, Z, and neutrons, N, was created.

The contribution of the budding field of quantum physics introduced the Pauli principle stating that no two particles with the same quantum numbers can occupy the same energy state. This introduction motivated the creation of a shell model for a nucleus held together by the short-range nucleon-nucleon interaction. Protons and neutrons can pair in three ways, n-n, p-p, and n-p. Same nucleon pairing must have opposite spins due to the Pauli principle, leading to same nucleon pairings having spin $I = 0$. The p-n pairing can have spin $I = 0$ or $I = 1$. The spin $I = 1$ state is the slightly tighter bound state and the reason for the existence of deuterons.

The nuclidic table is created by plotting the number of protons in a nucleus against the number of neutrons. All known elements are represented in the table. At low mass numbers, where the Coulomb energy is lowest, the line of stability coincides with the $N = Z$ line. The line of stability is a line that indicates the stability of nuclei in the table. For states outside the line of stability the nucleus will decay to reach the line, often by β^+ or β^- or α decay. With increasing Z the Coulomb force gains more relevance causing the line of stability to deviate from the $N = Z$ line for heavy nuclei $A \gtrsim 50$. The $N = Z$ line is a region of interest to study due to the relative stability of nuclei which fall in this region.

Technological advancement has led to the creation of ever improving particle accelerators which has allowed for the bombardment of a nuclei by other nuclei. This can give rise to fusion-evaporation reactions. The typical evaporates seen over the last 90 years are protons, neutrons and α particles. Gamma-ray spectroscopy is the technique used to analyse the reaction products, or recoils, in its extreme state of excitation energy and angular momentum. Fusion evaporation is commonly performed in order to create compound nuclei on the $N = Z$ line of the nuclidic table.

During the 2020 summer experimental campaign at Argonne National Laboratory (ANL) [1], a CD-shaped DSSD [2] was used as a telescope detector inside the Microball [3]. As a result of the increased energy granulation provided by the DSSD one could clearly discriminate between proton and deuteron evaporation. The main reaction of concern for this thesis is the fusion-evaporation reaction of ^{40}Ca and ^{24}Mg resulting in the production of the ^{64}Ge* compound nucleus. Comparison is performed between the two-proton-one-neutron (2pn) to deuteron-proton (dp) evaporation for ^{64}Ge* and the two contamination reactions resulting in the formation of the ^{56}Ni* and ^{52}Fe* compound nuclei. The α-proton-neutron (αpn) against the α-deuteron (αd) evaporation channel is also analysed for ^{64}Ge*.

2 Theory

2.1 Fusion-evaporation reactions

Fusion-evaporation reactions are a useful tool for creating nuclei with large angular momentum and excitation energy. Heavy ions are accelerated to typically have energies of the order of 3-5$\sim$ MeV per nucleon. At such energies the ion beam has enough energy to overcome the Coulomb barrier of impeding nuclei and so the most probable outcome is fusion between the two nuclei. The resulting

compound nucleus is in a state of high angular momentum and excitation energy. Ejecting or 'evaporating' a combination of protons, neutrons, deuterons, and α particles from the nucleus is the most energetically efficient way for the fused compound nucleus to release energy. What combination and quantity of the aforementioned evaporates are released is probability dependent. Evaporation occurs at approximately 10^{-19}s after fusion. Once it is no longer energetically favourable to evaporate particles, statistical γ rays are released from the recoil at approximately 10^{-15}s and continues until the the excitation energy reaches a minimum for the angular momentum of the recoil, known as 'yrast'. After reaching the yrast line discrete γ rays are released from the recoil as it strives to reach its ground-state energy. A typical time scale of the complete fusion-evaporation reaction is on the order of pico to nanoseconds.

2.2 Discrete γ-ray emissions

Discrete γ rays are released from an excited nucleus. The shell model describes the inner state of a nucleus in an analogous way to electron shells. The model accurately predicts the 'magic numbers' of protons and neutrons. The energy states nucleons occupy in the shell model are classified by quantum numbers, parity, and spin. Nucleons that de-excitate in energy give rise to electromagnetic multi-pole transition. The probabilities for the transitions to occur are governed by parity and angular momentum. The angular momentum takes integer values from the quantum mechanical addition of the initial and final state. Conservation of energy and momentum dictate that the γ-ray energy is practically equal to the difference of excitation energies between the states and the loss of angular momentum, respectively.

2.3 γ ray interaction in matter

The photoelectric effect, Compton-scattering, and pair production are the three main processes how γ rays interact in matter. The order denotes the importance for increasing photon energy. The attenuation coefficient denotes the total probability for a photon to interact with matter at different energies. This is illustrated in Figure 1. It is the superposition of the cross sections for the above three processes.

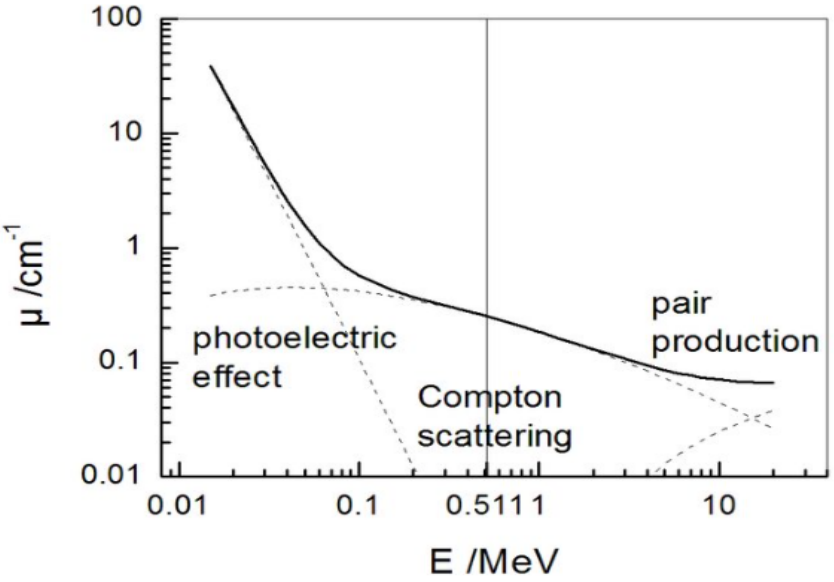

Figure 1: The attenuation coefficient of the photoelectric effect, Compton scattering, pair production and the total attenuation coefficient for anhydrite. The Figure is from [4].

2.3.1 Photoelectric effect

The photoelectric effect is an ionization process where the γ ray is fully absorbed by an inner bound electron. The electron is released from the nucleus with kinetic energy equal to the difference of the γ ray and its atomic binding energy. Another electron may de-excitate to fill in the hole left by ionization, releasing either an X-ray or Auger electrons.

2.3.2 Compton scattering

Compton scattering is an interaction between a photon and generally a valence electron. The photon with incident energy E_γ scatters off the electron, the photon looses energy from the interaction with a final energy E'_γ while the electron receives the lost energy in the form of kinetic energy. Utilizing conservation of energy and momentum one can show the scattering photon has energy,

$$E'_\gamma = \frac{E_\gamma}{1 + (E_\gamma / m_e c^2)(1 - \cos\theta)}$$

θ is the scattering angle of the photon and m_e the mass of an electron. Continuous applications of this process creates a continuum of energies which is the main form of background for γ-ray spectra.

2.3.3 Pair production

Pair production is the creation of an electron-positron pair from the full energy of the γ ray. The threshold for pair production occurs at the mass energy of the pair $1.022 \sim$ MeV. Any excess energy of the γ ray is converted into kinetic energy for the electron-positron pair. The kinetic energy will be deposited in the medium, while the positron will annihilate with an electron releasing two 0.511-MeV γ rays.

2.4 Heavy charged particles interaction in matter

Protons, deuterons, and α particles move with their electric field interacting with impeding atoms. The Coulomb force generated between these relatively heavy charged particles and electrons cause a transfer of momentum to the less massive electrons which receive some kinetic energy and ionize the impeding atoms. Ionized electrons which receive a relatively large quantity of kinetics energy may also cause further ionization. Many such interactions are often required to fully stop a heavy charged particle. A string of ionizations are the remnants of the heavy charged particle's energy. The rate of energy deposition depends on the stopping material, described by the Bethe-Bloch formula.

$$-\frac{\partial E}{\partial x} = \left(\frac{ze^2}{4\pi\epsilon_0}\right) \frac{4\pi Z \rho N_A}{A m_e v^2} \left(ln(\frac{2m_e v^2}{I}) - ln(1-\beta^2) - \beta^2 \right)$$

$\beta = v/c$ which accounts for relativity, m_e the mass of an electron, I the mean energy to ionize an atom, N_A Avogadro's number, ρ, A and Z the density, mass number, and proton number of the stopping material and ze the electronic charge of the relatively heavy charged particle.

2.5 Neutron interaction in matter

The main forms for neutron interactions in a medium are scattering and absorption. Scattering exchanges momentum to the medium. The neutron looses kinetic energy with each subsequent interaction and thermalizes. Cross section of absorption for low-energy neutrons tend to be larger, therefore these thermal neutrons are more easily absorbed. The daughter nucleus is created in an excited state corresponding to the binding energy and the initial kinetic energy of the neutron. For further detail of interaction of radiation in matter see [5].

3 Experimental Campaign

This thesis utilizes data collected over a three-month long experimental campaign conducted at Argonne National Laboratory (ANL) in 2020. Several experiments were conducted over this time, of which, the experiment of interest for this thesis is a heavy ion beam of ^{40}Ca with energy 106 $\sim$ MeV that was incident on a thin foil of ^{24}Mg. This causes fusion into the highly excited ^{64}Ge* compound nucleus which promptly evaporates light particles. The evaporates of interest for this thesis are protons, neutrons, deuterons, and α particles. The evaporates were detected by the Neutron Shell [6], Microball, and CD-shaped Double-sided Si-strip detectors (DSSDs) and the emitted γ rays by the Gammasphere [7]. A more in-depth discussion of the experiment, detectors and the handling of data is presented in Section 3.1, 3.2, and 3.3, respectively.

3.1 The experiment

3.1.1 Reaction

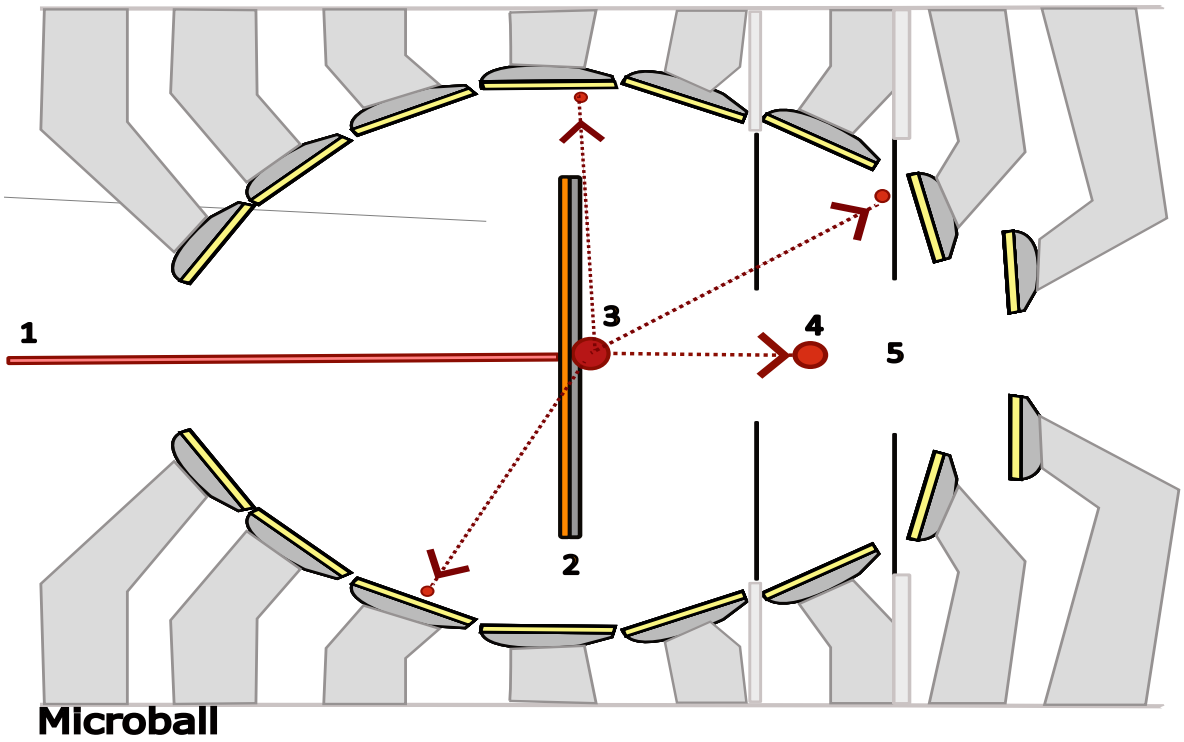

Figure 2: An illustration of the fusion-evaporation reaction inside the Microball. The red rectangle is below the label 1 represents the ^{40}Ca beam. The ^{24}Mg target is above the label 2 coloured in gray. The orange layer represents contamination on top of the Mg target such as ^{12}C and ^{16}O. 3 represents the compound nucleus produced from fusion. For the main reaction it is ^{64}Ge*. 4 represents the recoil which is ^{61}Zn for the main reaction . 5 is in between the two black rectangles which represent the outer two CD-shaped DSSDs. The surrounding detectors are the Microball rings. The red arrows pointing to the small circles represent the evaporates for the 2pn evaporation channel.

The experiment of interest was the fusion-evaporation reaction between a heavy ion beam ^{40}Ca incident on a thin sheet of ^{24}Mg. A general explanation for fusion-evaporation reactions is discussed in Section 2.1. The Mg target foil was placed at the inside the Microball chamber at its center. The Argonne Tandem Linac Accelerator System (ATLAS) accelerated the heavy ion beam of ^{40}Ca to an energy of 106-MeV. A schematic of the events in the Microball [3] is illustrated in Figure 2. The ^{40}Ca overcomes the Coulomb barrier of the ^{24}Mg allowing for collision and prompt fusion.

The result is the production of the compound nucleus ^{64}Ge*. The compound nucleus may follow many possible decay paths. This bachelor thesis focuses on four main channels 2pn, dp, αpn, and αd. The resulting recoil of the former is ^{61}Zn while the later results in ^{58}Cu. The evaporation channels of interest are displayed in Figure 3.

$$^{40}\mathrm{Ca} + {}^{24}\mathrm{Mg} \longrightarrow {}^{64}\mathrm{Ge}^* \begin{cases} \nearrow {}^{61}\mathrm{Zn}^* + 2\mathrm{p} + \mathrm{n} \\ \nearrow {}^{61}\mathrm{Zn}^* + \mathrm{p} + \mathrm{d} \\ \searrow {}^{58}\mathrm{Cu}^* + \alpha + \mathrm{p} + \mathrm{n} \\ \searrow {}^{58}\mathrm{Cu}^* + \alpha + \mathrm{d} \end{cases}$$

Figure 3: The four evaporation channels of interest for ^{64}Ge*.

$$^{40}\mathrm{Ca} + {}^{16}\mathrm{O} \longrightarrow {}^{56}\mathrm{Ni}^* \begin{cases} \nearrow {}^{53}\mathrm{Fe}^* + 2\mathrm{p} + \mathrm{n} \\ \searrow {}^{53}\mathrm{Fe}^* + \mathrm{p} + \mathrm{d} \end{cases}$$

$$^{40}\mathrm{Ca} + {}^{12}\mathrm{C} \longrightarrow {}^{52}\mathrm{Fe}^* \begin{cases} \nearrow {}^{49}\mathrm{Cr}^* + 2\mathrm{p} + \mathrm{n} \\ \searrow {}^{49}\mathrm{Cr}^* + \mathrm{p} + \mathrm{d} \end{cases}$$

Figure 4: The evaporation channels of interest for ^{56}Ni* and ^{52}Fe*.

The Microball was kept in near vacuum conditions to limit unwanted ion beam collisions. The vacuum was not perfect and as a result contaminates were present on the Mg sheet. The contaminants of interest for this thesis are ^{12}C and ^{16}O. Fusion with the ion beam resulted in the production of the compound nuclei ^{52}Fe* and ^{56}Ni*, respectively. As displayed in the Figure 2 the contaminants formed a thin cover over the Mg sheet leading to fusion evaporation reactions between the contaminants and beam. The evaporation channels of interest for the compound nuclei ^{52}Fe* and ^{56}Ni*, for this thesis are the 2pn and dp evaporation channels. The decay channels of interest for these contamination reactions are displayed in Figure 4.

The recoil after reaching yrast releases γ rays that are Doppler shifted due to the velocity of the recoil. Discussion of the detection of the evaporates and γ rays along with corrections to the Doppler broadening are contained within Section 3.2 and 3.3, respectively.

3.2 Experimental setup

The fusion-evaporation reaction occurring inside the Microball is discussed in Section 3.1. The charged evaporates are meant to be detected by either the Microball or the CD-shaped DSSDs contained within the Microball. The DSSDs were used as a telescope detector allowing for improved particle discrimination over the Microball. The Microball is contained within the Gammasphere which was surrounded by anti-Compton Bismuth germanium oxide (BGO) detector shields. The Gammasphere detected the discrete γ rays released by the recoil. Neutrons released from evaporation can be detected by the Neutron Shell which replaced parts of the Gammasphere. A Fragment Mass Analyser (FMA) [8] was present to determine the nature of the recoil. This paper omits using data collected from the FMA due to its small detection efficiency causing a reduction of statistics. The nature of the recoil was instead identified by analysis of the detected evaporates and coincident γ rays. This process is described in Section 4.

3.2.1 Gammasphere

The Gammasphere consists of up to 110 High-Purity Germanium (HPGe) detectors arranged to have a near solid angle coverage of 4π [9]. 69 of the 110 HGPe detectors were operational during the experiment. 32 of the 110 were replaced by the Neutron Shell . HPGe is a type of semi-conductor

detector. Such detectors are created by connecting p-doped and n-doped semi-conductors creating a neutral depletion zone at the boundary of contact. The positive p-doped side and the negative n-doped side surround the depletion zone resulting in an electric field. Applying a reverse bias increases the width of the depletion zone and detection zone. A γ ray entering may ionize atoms in the depletion zone resulting in fast electrons which creates a large number of electron and hole pairs along its slowing-down path. The electron and holes which are subsequently separated and moved by the electric field. The collected charges create a signal which is detected and recorded with surrounding electronics. The HPGe crystals were cooled with liquid nitrogen to prevent thermal crossings of germanium's relatively small band-gap.

Each HPGe crystal was surrounded by a BGO anti-Compton shield. A BGO detector acts as a scintillator detector. Scintillator detectors have good detection efficiency but rather poor energy resolution. The BGO detector helps to insure accurate γ-ray energies are detected. An accurate energy reading occurs if the γ ray deposits all its energy in the HPGe detector. In the case this does not occur the BGO detector is meant to detect the escaping γ ray. Detection of escaping γ rays facilitates selection of data only containing full-energy deposition in the HPGe detector.

For information on improvements made to the alignment of the HPGe detectors see the Masters thesis of Dalia Farghaly [10].

3.2.2 Neutron shell

As stated previously up to 32 of the possible 110 HPGe detectors were replaced by hexagonal liquid scintillator detectors with an approximate angular coverage between $10^\circ - 70^\circ$ with respect to beam direction. Neutron and γ-ray detection were discriminated by pulse-shape discrimination and time-of-flight.

3.2.3 Microball

A complete Microball is comprised of up to 95 Caesium-Iodide Thallium activated CsI(Tl) scintillation detectors and has a near 4π solid angle measurement coverage around the position of the target. The Microball is used to detect light charged particles such as protons and α particles. Discrimination between the evaporates were performed with standard pulse-shape discrimination techniques as well as with the charge-comparison method and the cosine similarity method implemented in the bachelor thesis of Linus Perrson [11]. Detection of these charged particles also allows for the direction of the recoil to be kinetically determined, which further allows for improved Doppler corrections for the detection of γ rays. The Microball has relatively low energy resolution and usually cannot discriminate between protons and deuterons. For better energy resolution one detection ring containing 12 CsI(Tl) scintillation detectors was replaced with two CD-shaped DSSDs.

3.2.4 CD-shaped DSSDs

The addition of two CD-shaped DSSDs into the Microball allows for higher granulation. It operates as a $\Delta E - E$ telescope. Both DSSDs have 32 rings and 64 sectors and therefore a granularity of 2048 pixels, the innermost with thickness 310µm and outer most with thickness 520µm. Both contained a circular hole at the center to allow for the recoils and the primary beam to pass into the FMA. The inclusion of these two CD-DSSDs allowed for the detection and discrimination of deuterons over protons. In the case of protons and deuterons with energies sufficient to punch through the DSSDs, the corresponding Microball rings were used as a third telescope. For further information on the implementation for discrimination between protons and deuterons with the two DSSDs see the PhD thesis of Yuliia Hrabar [12].

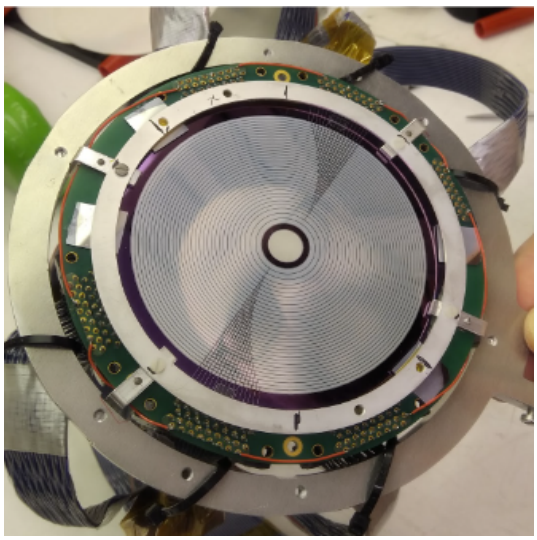

Figure 5: An image of the ring side of the CD-shaped DSSD.

3.3 Energy corrections

The detection of the energy of all detected evaporates allows for event-by-event Doppler corrections for γ rays detected in the Gammasphere. The moving recoil causes Doppler broadening for detected γ rays. For increased energy accuracy and resolution, a Doppler correction must be applied. In order to account for this the velocity vector of the recoil was determined by determining the total momenta of the evaporates and subtracting it from the initial total momentum of the compound nucleus. The momenta of the evaporates were found using the tracking capabilities of the detectors. The beam was assumed to travel perpendicular to the Mg target and the momentum of the beam allowed for the momentum of the compound nucleus to be determined. Conservation of momentum is utilized and the velocity of the recoil is then determined.
The energy of the γ rays are corrected according to the following equation,

$$E_\gamma = E_{\gamma 0}\left(1 + \frac{v}{c} cos\theta\right)$$

E_γ is the detected γ-ray energy, $E_{\gamma 0}$ is the energy of the γ ray without recoil movement, v the nucleus speed and θ the angle between the velocity vector of the recoil and γ ray. This formula is valid for non-relativistic motion.

4 Analysis Method

4.1 Background

This project focused on analysing ROOT [13] files that contained γ-γ matrices. The creation of these files was performed by Yuliia Hrabar and is detailed in her Phd thesis [12]. For each recoil a separate file was used as kinematic corrections were performed on the γ-ray energies as discussed in Section 3.3. Furthermore, each of the four recoils received an extra file due to different evaporate filtering as discussed in Section 4.1.1. A total of eight files containing γ-γ matrices were analysed throughout this project. A further explanation of the γ-γ matrix is presented in Section 4.1.2.

4.1.1 Filtering of γ-γ matrices

In total three γ-γ matrices were analyzed for each element. γ rays were filtered into the matrices by the detected evaporates. The selection is performed to reduce the number of unwanted γ rays

detected from all the possible recoils and to split up the deuteron decays from the proton-neutron counterpart. The conditions used for filtering are listed below.

- Evaporation channels which did not contain a deuteron required the detection of a proton in the two DSSDs. This condition was enforced to allow comparison with deuterons which could solely be discriminated by the DSSD and therefore both decay channels having a comparable solid-angle detection efficiency for charged particles.
- The desired evaporates from an evaporation channel must be detected in coincidence with the γ rays. This condition allowed for all recoils produced with the same evaporates to be isolated from other decay channels. A recoil is then discriminated by projecting on a known transition of the desired recoil. This condition is used in parts of this paper, however, the third condition was often preferred.
- The transitions that were gated on as discussed in Section 4.2 are often sufficiently unique such that the neutron detection condition can be dropped in some cases, such that only charged particle detection was sufficient. The deuteron evaporation channels in this paper do not contain additional neutron evaporation , however, naturally the pn counterpart does, and so the decay channels cannot be directly compared due to possibly varying efficiencies of neutron detection. Therefore, removing this condition facilitated a closer comparison between the deuteron and proton-neutron evaporation channels.

As a result of these conditions two files were produced. A file that solely contained charged evaporate filtering. This file contained substantially more statistics as discussed in Section 5.4, along with facilitating a closer comparison between deuteron evaporation and proton-neutron evaporation. The other file produced required charged and neutral evaporates to be detected. Statistics are lower in these γ-γ matrices, however, less background is also present, allowing for cleaner analysis.

4.1.2 The γ-γ coincidence matrix

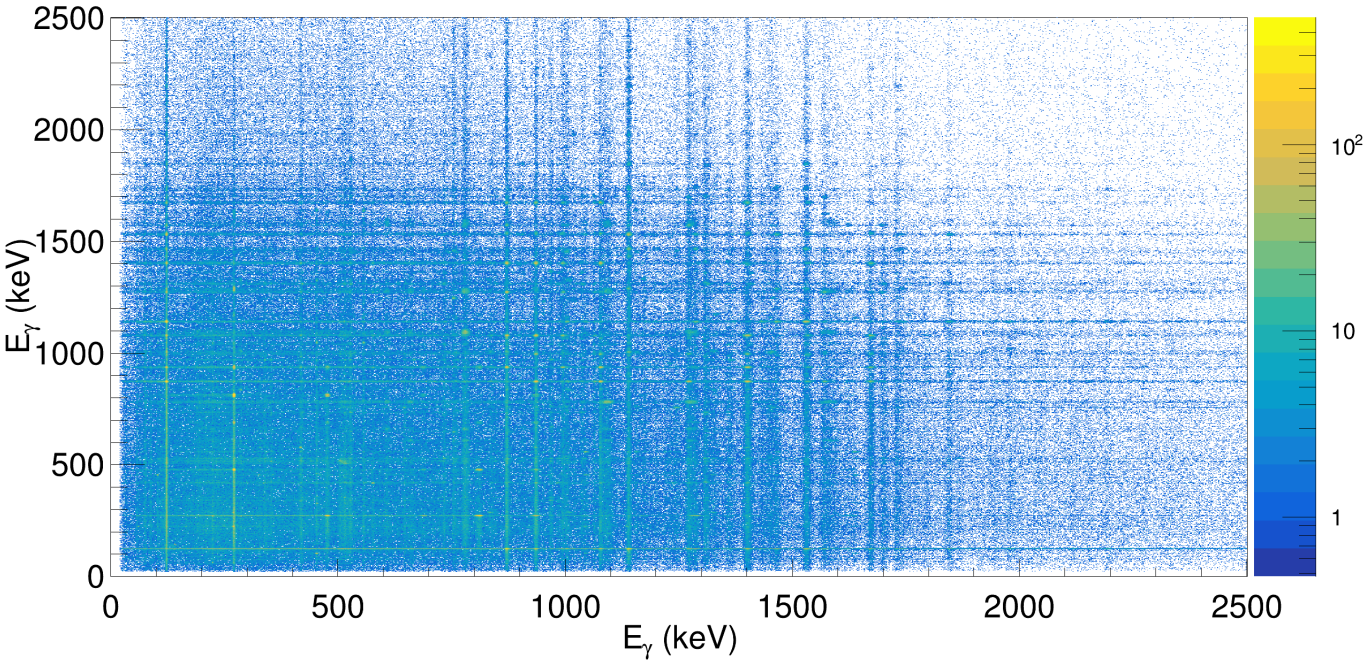

Figure 6: An example of a γ-γ matrix Doppler corrected for ^{61}Zn with a logarithmic applied to the Z-axis. Brighter horizontal or vertical lines correspond to coincidence spectra.

A γ-γ matrix is a two dimensional histogram with γ-ray energy plotted on the X and Y-axis. The plot is populated by counts of detected coincident γ ray. The matrix is invariant to X and Y-axis

inversion. The time condition applied to γ ray condition causes all γ rays in the matrix to be coincident to some other γ ray. An example matrix is displayed in Figure 6 with a logarithmic scale applied to the Z-axis. To read the matrix one chooses the X or Y-axis as a reference point, for this example the X-axis is used. The vertical lines perpendicular to the X-axis represent a collection of γ-ray energies that were detected in coincidence to the γ ray with the energy of that point on the X-axis. The majority of these γ rays originate from background processes. Lines that are brighter correspond to different coincidence spectra. Figure 7 displays a enhanced section of the coincidence matrix. The light blue line running perpendicular to the X-axis at 124-keV contains the general background processes seen for the decay of ^{61}Zn, the most prominent of which is Compton-scattering. The dark blue background represents a general background. The red boxes display the 873-keV and 1147-keV coincident transitions which are in the lower energy region of the ^{61}Zn decay scheme, represented in Figure 11. The transition is yellow due to the large density of counts as such coincident transitions are typically in areas with a larger density of counts.

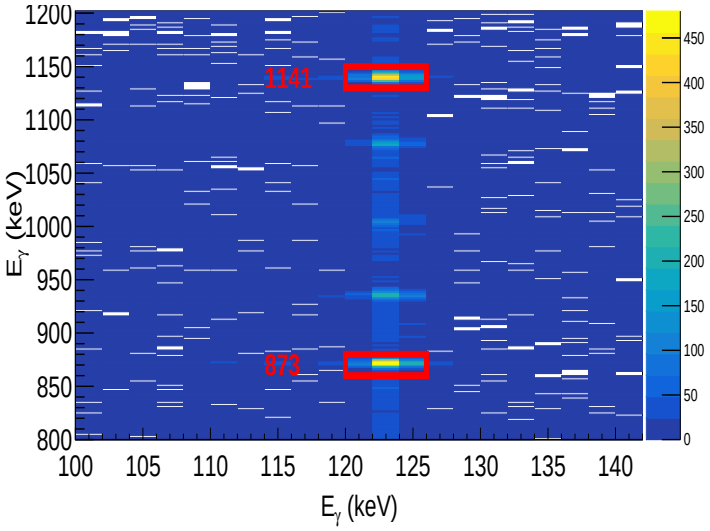

Figure 7: Example of coincidence γ rays to the 124-keV ground-state transition of ^{61}Zn. The red boxes indicate coincident transitions at energies of 873-keV and 1141-keV.

4.2 Productions on γ-ray coincidence spectra

Projections on γ-γ matrices produce γ-ray spectra that omit γ rays detected from unwanted reactions. This is achieved due to the time condition placed on the detection of γ rays in the HPGe detector, resulting in the recording of only coincident γ rays. A general background removal was also achieved by utilizing projections to create cleaner coincidence γ-ray spectra. The code was written in C/C++ and ran in the ROOT environment.

4.2.1 Projections

The γ-γ matrix is composed of a series of 2-keV energy bins. If the energy of a γ ray is within this region a count is assigned to this bin. A projection selects a number of these bins and super-imposes the counts assigned to the selected energy 'gating'. All projections are performed on the Y-axis with gatings on the X-axis. A known γ-ray energy of the recoil is selected and gated upon. The selection of the transition followed two criteria.

- The transition contained a high quantity of counts. Often the peak resulted from a transition to the ground-state.
- The transition energy was isolated from other energy transitions, allowing for lesser contamination and cleaner background removal. As such low-energy transitions were preferred.

Using the above conditions allowed for the creation of coincidence γ-ray spectra. The choice of gating remained consistent across the dp and 2pn γ-γ matrices.

4.2.2 Background removals

With all experiments a general background exits. Assuming that the background is approximately constant over small energy intervals allows for a general background removal. Background projections were gated either side of the peak of interest and multiplied with a weighting factor after which the background sections were negatively superimposed on the selected transition projection in order to remove the general background. For proton-neutron and deuteron evaporation channels the projection gating was consistent for the same recoil. Table 8 contains the gating energy range for the peak and background projections used for the different recoils. An example of such a removal process is displayed in Figure 8. The figure displays the projection of the 124-keV ground-state transition of ^{61}Zn as well as the two weighted background spectra with conditions that all neutral and charged evaporates were detected for the creation of the γ-γ matrix. A coincidence spectrum with background removed is displayed in Figure 10.

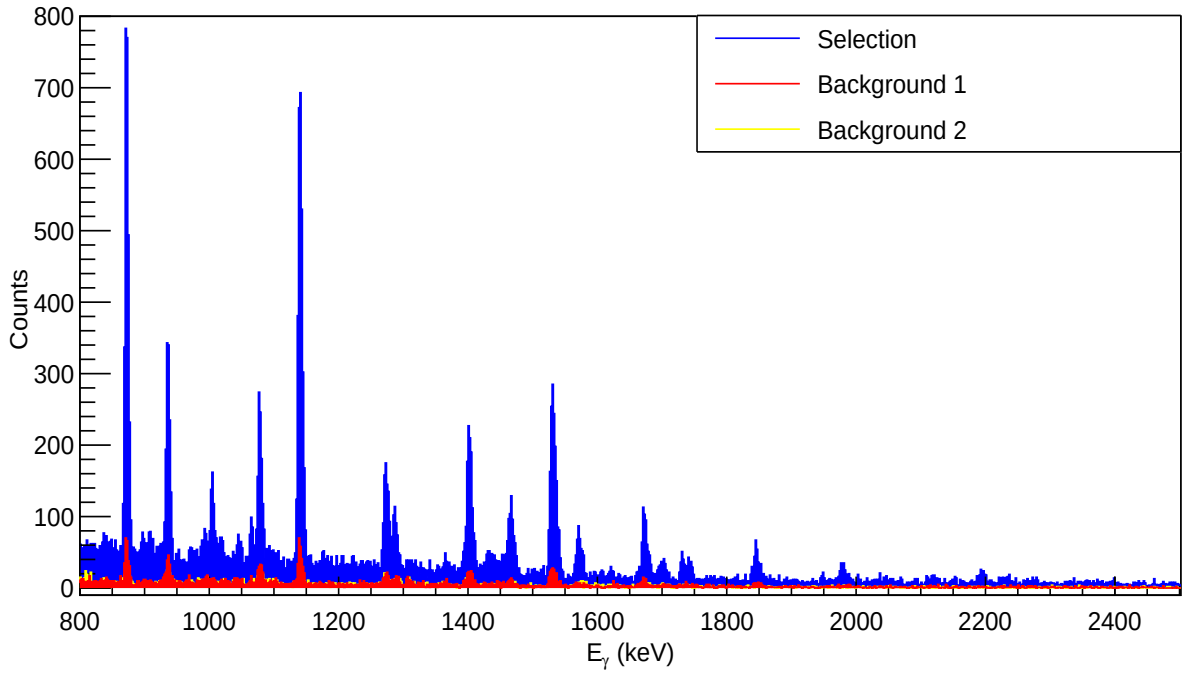

Figure 8: ^{61}Zn γ-ray spectrum in coincidence with 124-keV emission. Blue, the initial projection [120-126-keV]. Red and yellow, the background [114-120-keV] and [126-132-keV] both with a normalization factor of 0.5.

4.3 Determining intensities

The intensities of the peaks in the γ-ray coincident spectrum allow for comparison between the evaporation channels. The intensities were measured using the integration method of the peak fitting package hdtv [14]. A region of integration around the desired peak is selected along with a background region either side of the peak. The background regions averages the height of the background for the two regions, subsequently a line between the two background heights is created which intersects the region of integration. The program then determines the total intensity of the region by integrating everything in the integration region and background intensity by separately integrating everything in the integration peak below the line of the background. The peak intensity is determined by removing the background from the total intensity.
The background and integration regions selections were kept consistent for proton-neutron and

deuteron spectra. The intensities of each identifiable peak in the coincidence spectra were determined using this method and are tabulated in the Appendix. Figure 9 displays the integration and background region for the 873-keV coincident γ ray peak for ^{61}Zn.

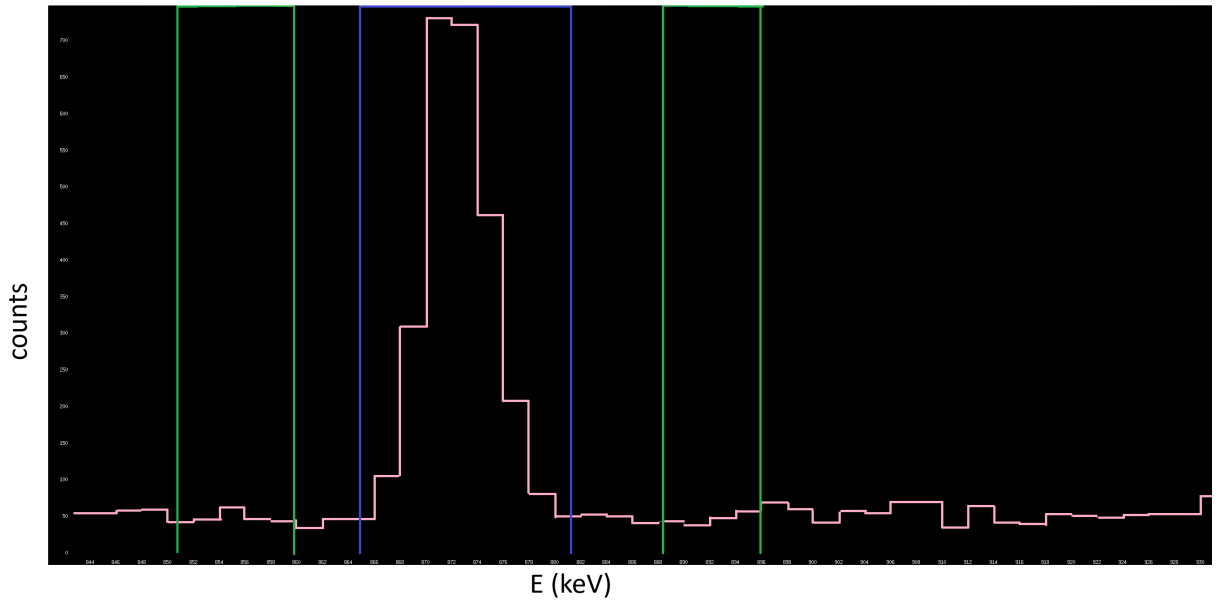

Figure 9: hdtv integrating the 873-keV transition in ^{61}Zn. The blue region represents the integration region. The two green regions represent the selected background regions.

5 Results

5.1 ^{61}Zn

The coincidence γ-ray spectra created from gating on the 124-keV transition of ^{61}Zn for the 2p and dp γ-γ matrices are displayed in Figure 10. Gating upon the 124-keV transition with 2p settings isolates γ rays from the 2pn evaporation channel. The quantity of counts on the Y-axis indicates the strong preference for the decay of a proton-neutron pair over a deuteron. The relative strength of the energy peaks are also apparent when viewing the spectra. Let the strongest 837-keV peak be the reference point for both spectra. It is apparent that the 937-keV, 1079-keV, 1289-keV, 1466-keV, and 1675-keV peaks are relatively stronger in the dp spectrum compared with the 2p spectrum. Therefore, these spectra indicate that a proton-neutron decay compared to a deuteron decay causes the recoil to populate different energy and spin states at differing rates.

The intensity of each resolvable peak was measured and tabulated for the 2p, 2pn, and dp γ-ray spectra in Table 3. The dp γ-ray spectrum contains seven less resolvable peaks than the the 2p spectrum. Each of these seven peaks are relatively weak in the 2p and 2pn spectra. This indicates that the absence of these peaks from the dp spectrum is most likely a result of the dp spectrum containing substantially lower statistics than the 2p and 2pn spectra. It is also of note that the peaks centered at 1731-keV and 1741-keV formed a doublet for the 2p spectrum and so the corresponding intensities may be inaccurate. The doublet is resolvable in the dp and 2pn spectra. The relatively lower intensity yield in the 2pn spectrum compared to the 2p spectrum is a result of the efficiency of neutron detection.

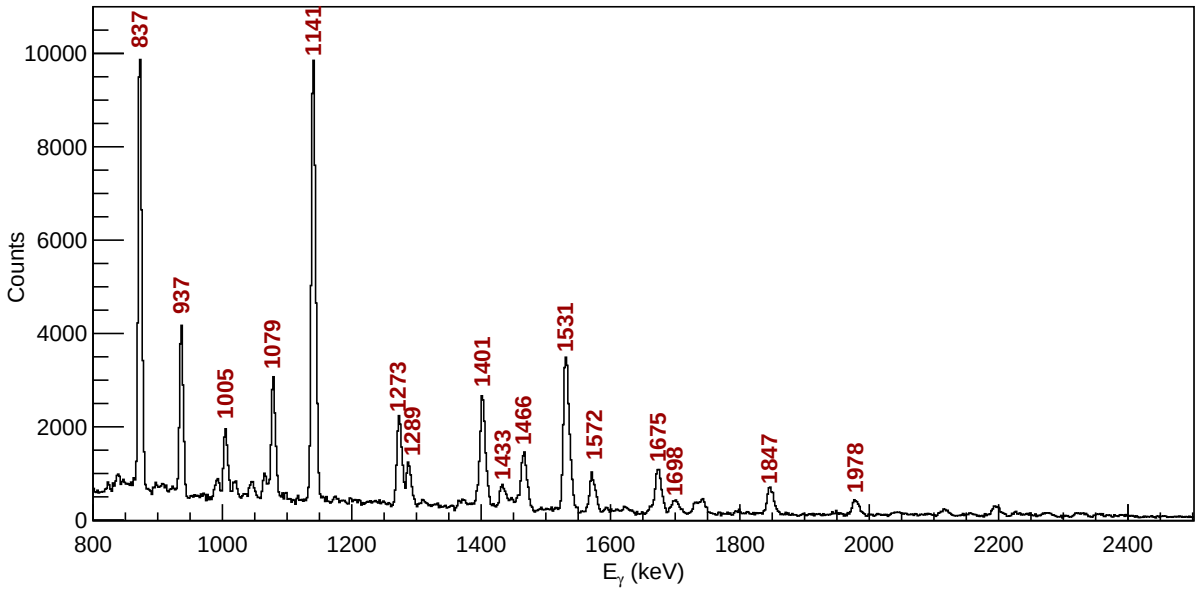

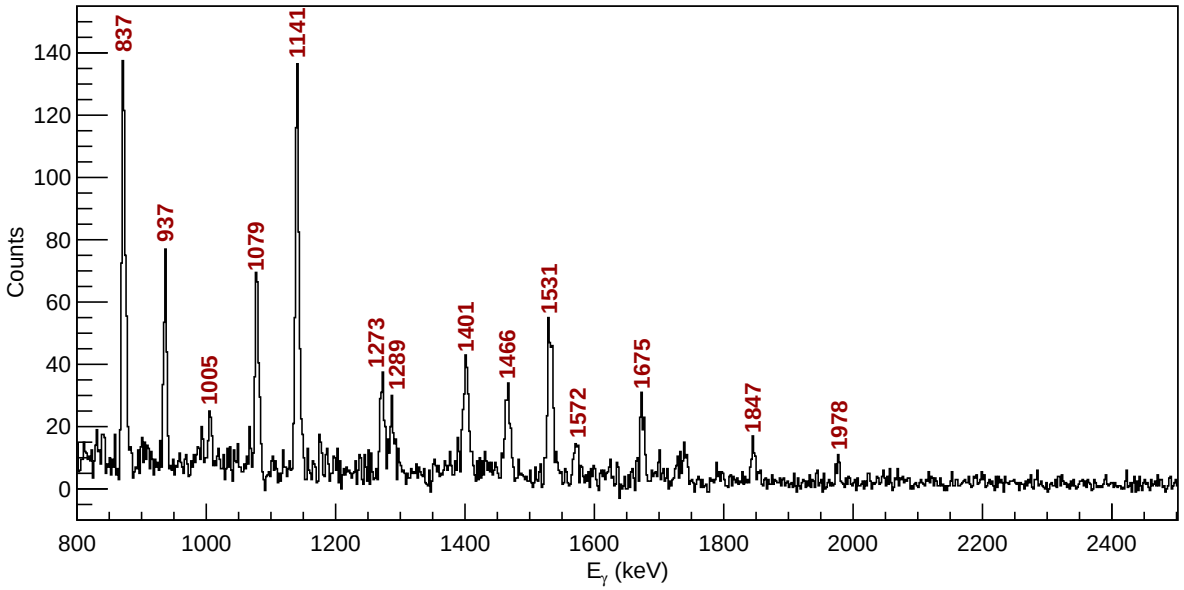

Figure 10: The graphs contain the γ-ray coincidence spectra for the two evaporation channels of ^{61}Zn produced from gating on the 124-keV transition. (Top) The 2p spectrum corresponding to the 2pn evaporation channel. (Bottom) The dp spectrum. The red text indicates identified transitions that are labelled with their energies in keV.

Figure 11 displays the decay scheme for ^{61}Zn [15]. The thickness of the black lines indicate the relative strength of a transition. The blue arrows indicate transitions seen in all spectra and the yellow arrows indicate transitions that were not resolvable in the dp spectrum as discussed earlier. The majority of the lower energy levels within the main decay branches are observed. With exception of the 997-keV transition. This is expected since it is parallel to the 124-keV transition as a ground-state transition and therefore will not be in coincidence. The seven peaks that could not be resolved are indicated with the yellow arrows. Six of which are transitions which connect branching decay channels, while, one connects to the $25/2^{-1}$ spin state at 8879-keV excitation energy. This peak was the weakest of the all resolvable peaks in the 2p spectra. So as would be expected, it is absent in the 2pn and dp spectra. The absence in the 2pn spectrum further suggests the absence in the dp spectrum is a result of lower statistics.

The relative intensity of the transitions in the dp spectrum compared to the 2p and 2pn spectra are plotted against spin and excitation energy in Figure 12. It appears that for larger spin and excitation energy the relative strength of dp to 2p and 2pn peaks increases. A linear fit was applied and is indicated by the red line with an uncertainty region in a faint red. Within the uncertainty regions the majority of data points fall into the fit. The fit appears to give a decent approximation of the trend. The fitting parameters are tabulated in Table 7.
The relative intensity of peaks from the 2pn spectrum compared to peaks from the 2p spectrum were plotted against spin and excitation energy and are displayed in Figure 13. It is expected that the condition for neutron detection would decrease the statistics by a constant. Therefore, a horizontal line would be expected. However, the linear fit performed is slightly sloped.

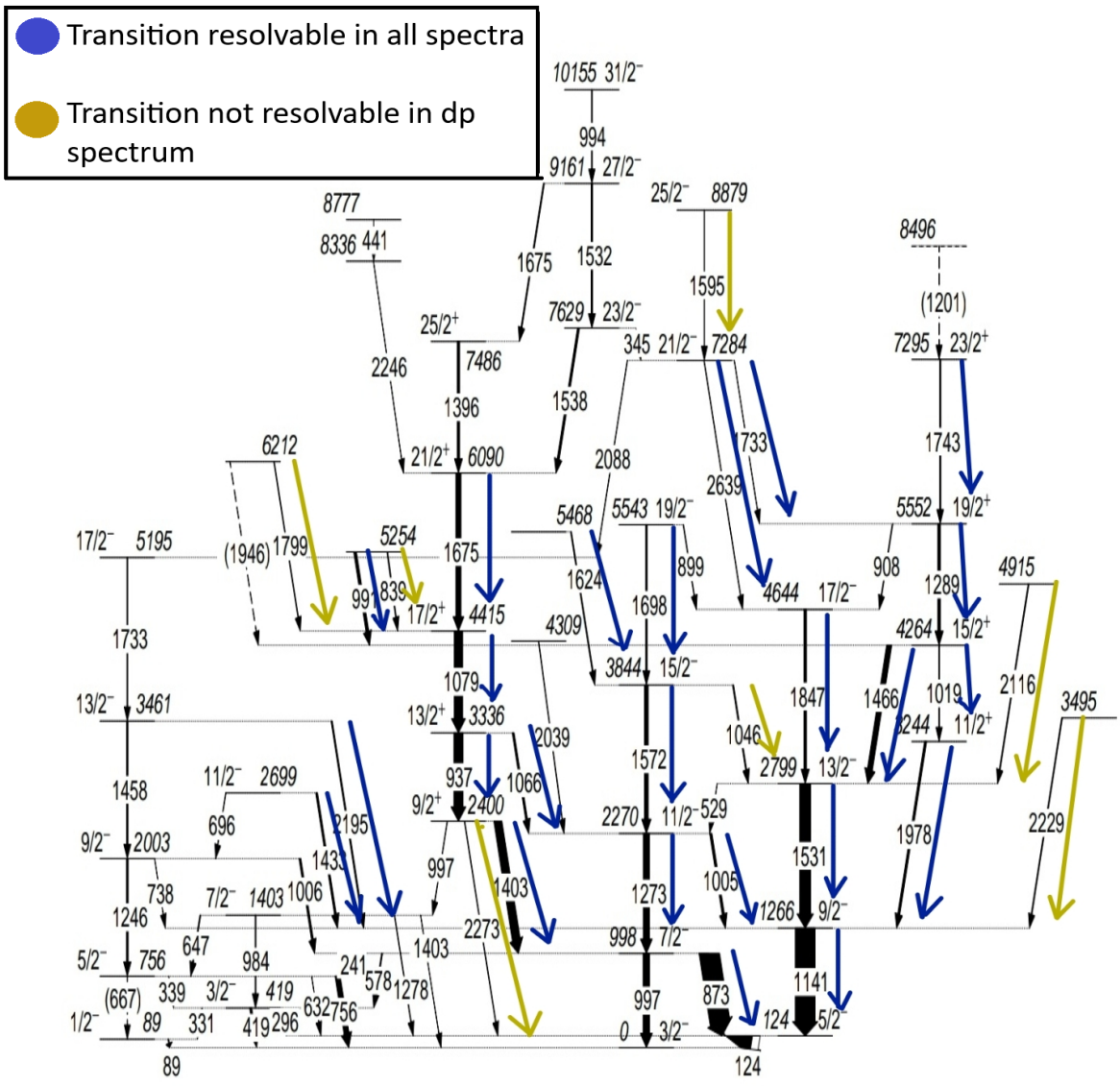

Figure 11: The decay scheme for ^{61}Zn adapted from [15]. The blue arrows indicate resolvable transitions in the 2p, 2pn, and dp spectra. The yellow arrows indicate transitions not seen in the dp spectrum.

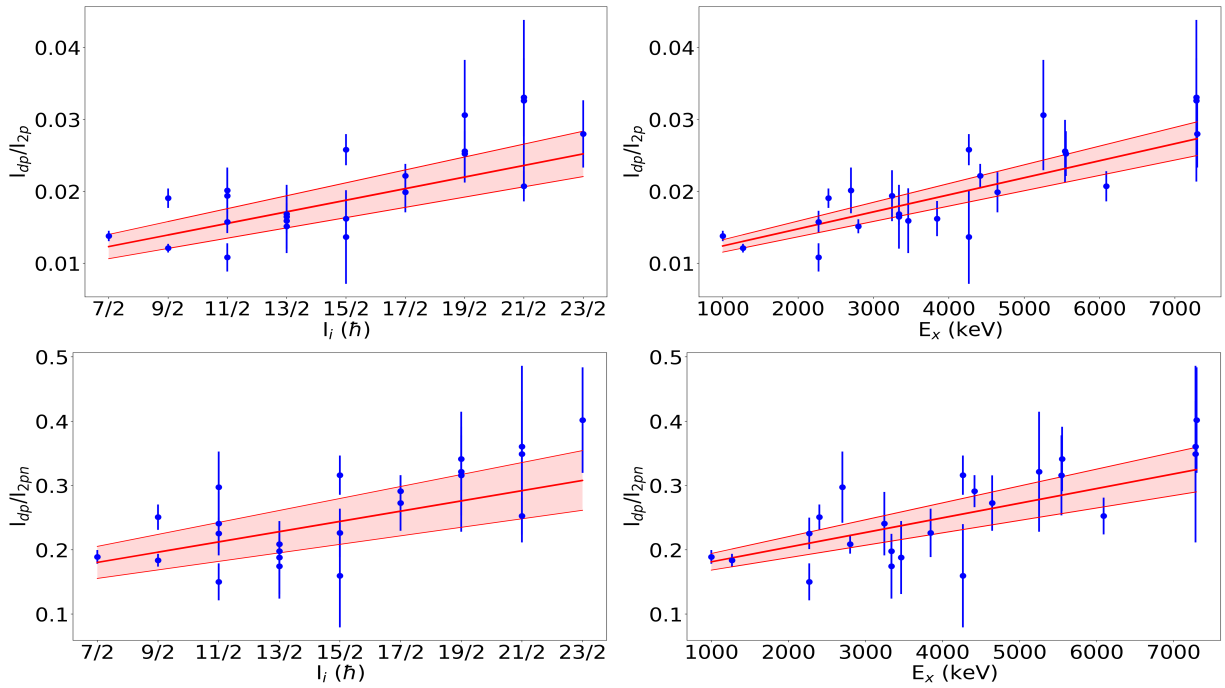

Figure 12: The relative intensities of peaks in the coincidence spectrum with dp settings against the 2p and 2pn spectra for ^{61}Zn. The top row is for 2p and the bottom 2pn. The left is the ratio plotted against spin, I_i, and the right against excitation energy, keV.

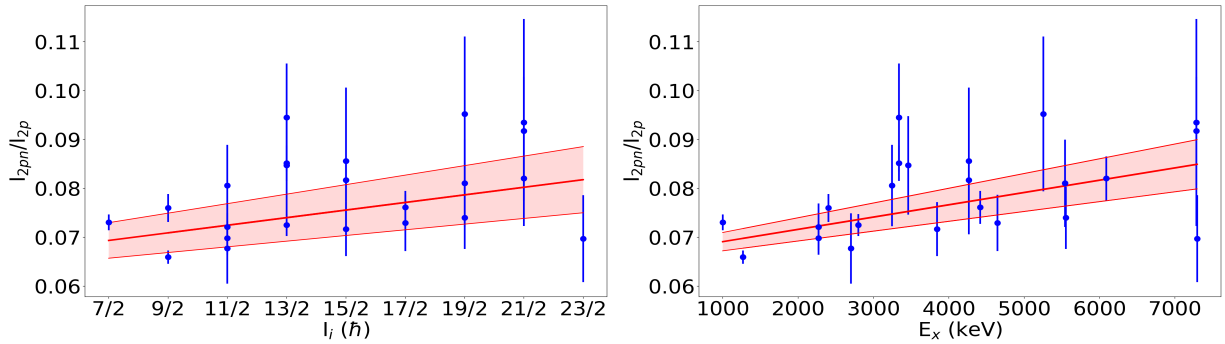

Figure 13: The relative intensities of peaks from the coincidence spectrum with 2pn settings against 2p spectrum for ^{61}Zn. (Left) The relative intensity plotted against the spin, I_i of the peak. (Right) Relative intensity plotted against the excitation energy, keV.

5.2 ^{58}Cu

Figure 14 displays the αp and αd coincidence γ-ray spectra created by gating on the 444-keV transition in ^{58}Cu. Comparing the counts for the αp spectrum to the 2p spectrum in Figure 10 illustrates how relatively weak the αpn to 2pn evaporation channel is. The αp spectrum is noisy with few resolvable peaks. The problem is amplified for the αd spectrum. Comparison of the two spectra reveals the relative strength of comparative peaks for the αp and αd differ. Notable examples are the 515-keV and 1356-keV transitions. However, judging visually on relative height may be misleading given the poor statistic for the ^{58}Cu αd spectrum.

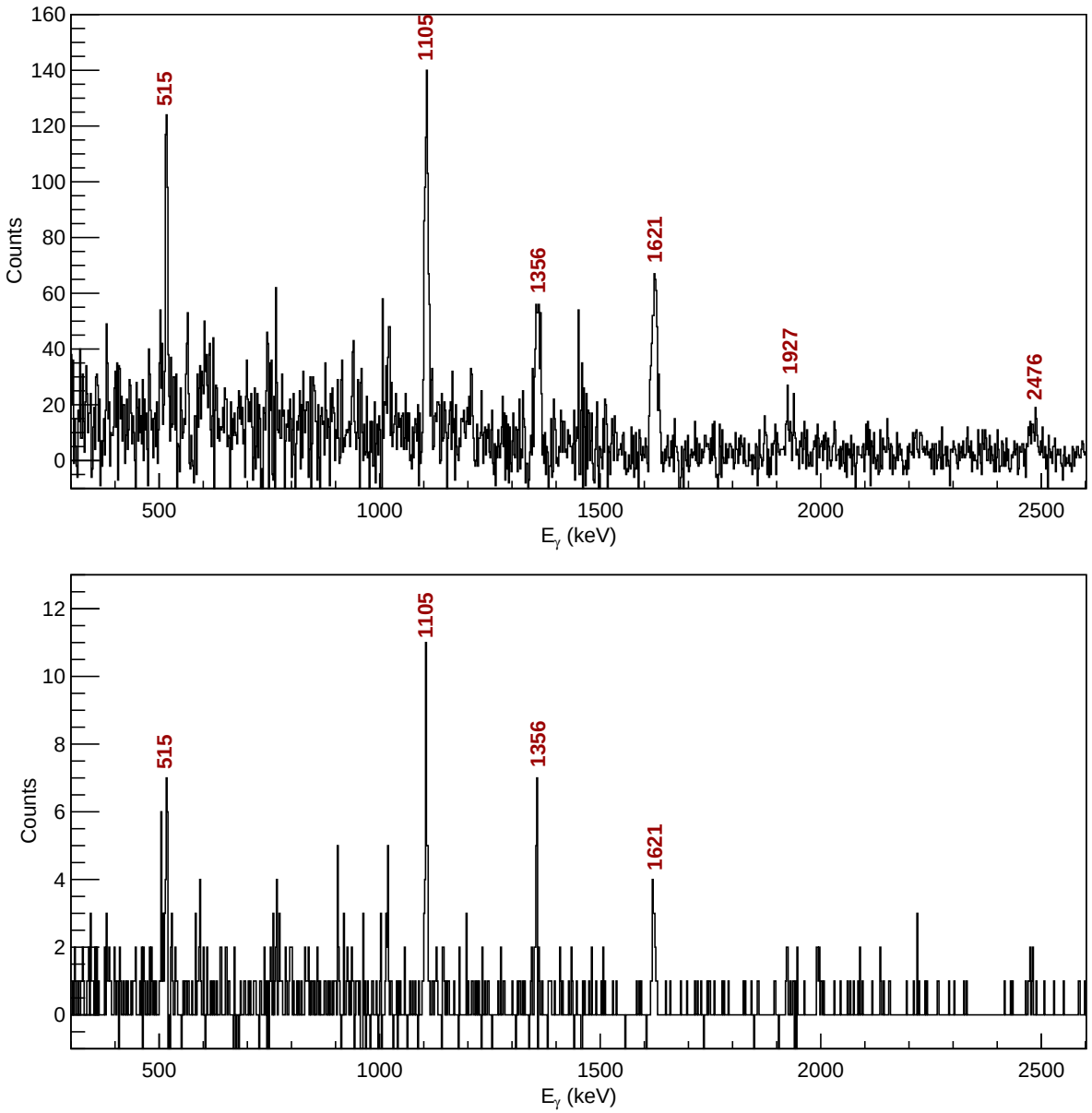

Figure 14: The γ-ray coincidence spectra for the two evaporation channels of interest for ^{58}Cu produced from gating on the 444-keV transition. (Top) The αp spectrum corresponding to the αpn evaporation channel. (Bottom) The αd coincidence spectrum. The red text indicates identified transitions that are labelled with their energies in keV.

The intensity of each resolvable peak for the αp, αpn, and αd spectra are tabulated in Table 4. A result of the low statistics is that few peaks are resolvable and contain relatively large statistical uncertainties in intensity yield. Figure 15 displays the decay scheme for ^{58}Cu [16]. Transitions seen in all channels are marked with blue arrows. The transition not seen in the αp spectrum is marked in purple. The fitted energy of the 501-keV varies largely across the three cases. The intensity yield is tabulated, however, is not used for the below analysis. The 906-keV transition is not observed in the αp spectrum. The transition was deemed to be resolvable for the αpn and αd, however, due to the weakness of the respective peaks and the transition not being resolvable in the αp spectrum the transition was not used for the below analysis.

The relative intensities of the αd to αp and αpn spectra are plotted against the spin and excitation energy of the transition as displayed in Figure 16. The fit appears to trend weakly upwards. However, as a result of the large uncertainties this is not conclusive. The fitting parameters are

contained in Table 7. The relative intensity of transitions from the αpn spectrum to αp spectrum are plotted against the spin and excitation energy of the transition in Figure 17. As is the case with ^{61}Zn one expects a horizontal line. The fit appears to have a slight slope but due to the large uncertainty, no definitive conclusion can be made.

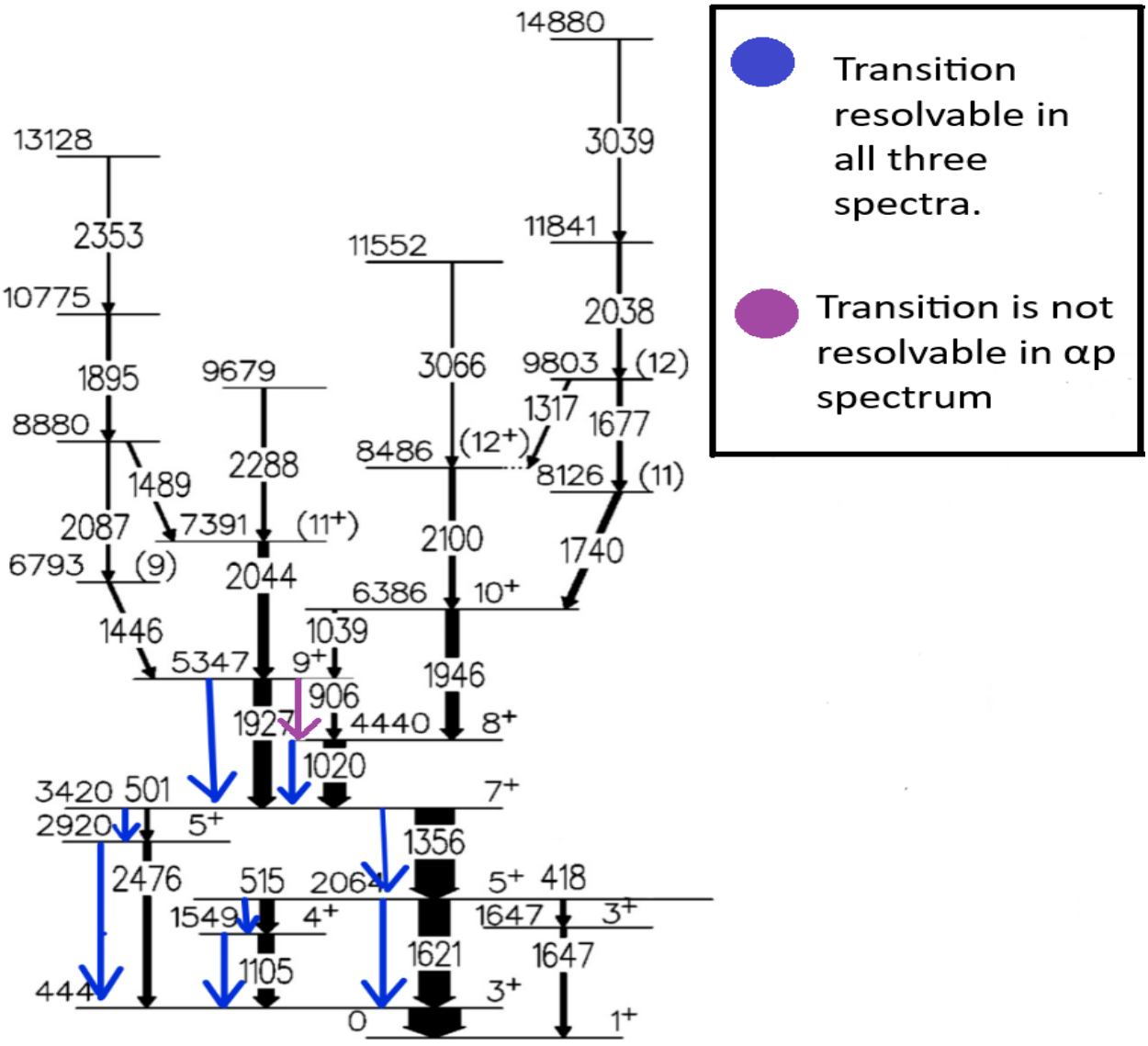

Figure 15: The relevant section of the decay scheme for ^{58}Cu adapted from [16]. The blue arrows indicate the transitions seen in the αp, αpn, and αd spectrum. The purple arrow indicates the transition not seen in the αp spectrum.

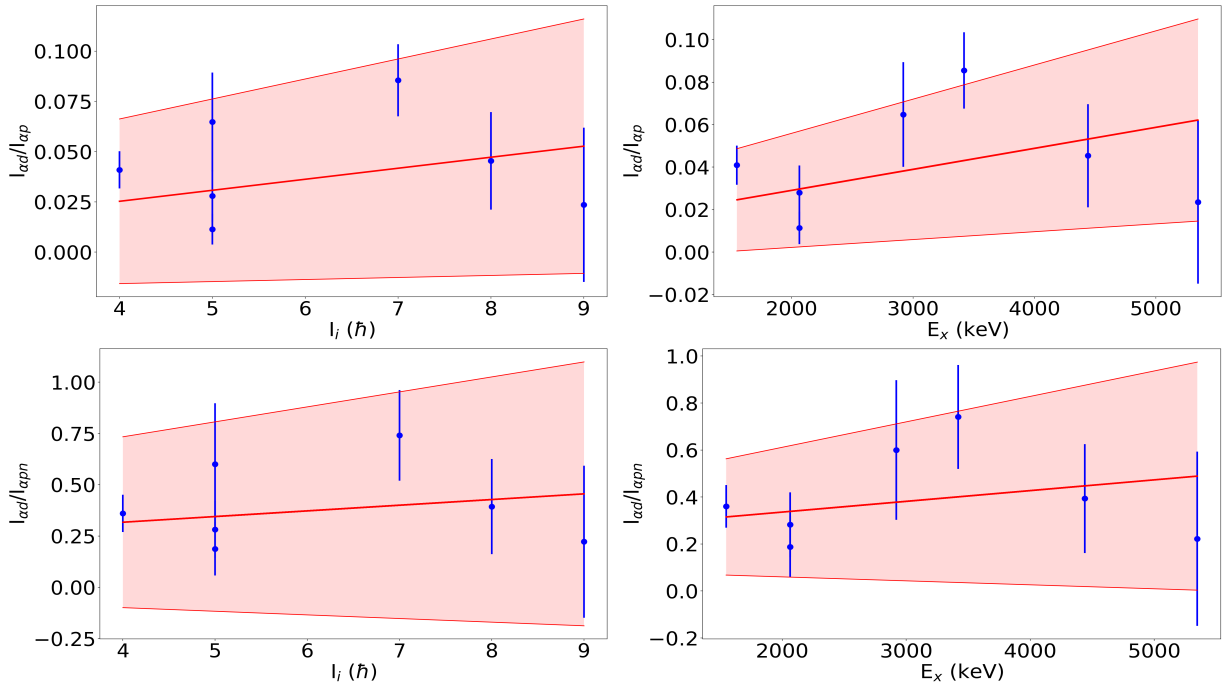

Figure 16: The relative intensities of peaks in the coincidence spectrum with αd settings against the αp and αpn spectra for ^{58}Cu. The top row is for αp and the bottom αpn. The left is the ratio plotted against spin, I_i, and the right against excitation energy, keV.

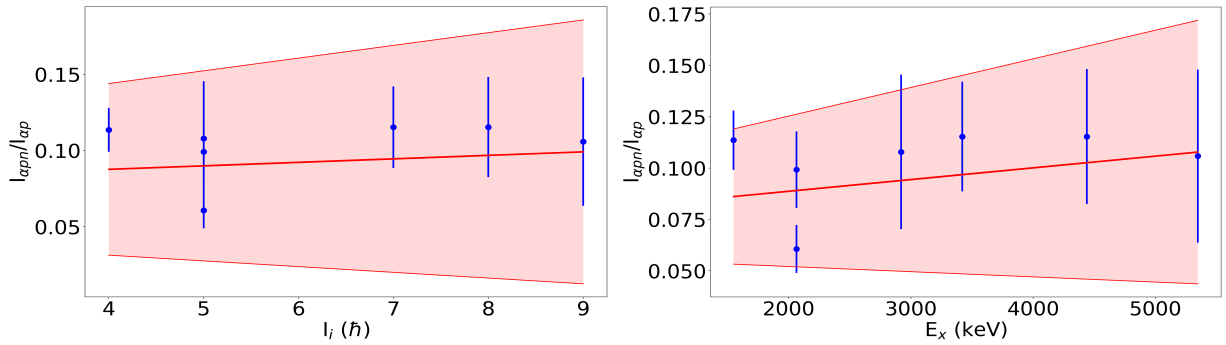

Figure 17: The relative intensities of peaks from the coincidence spectrum with αpn settings against αp spectrum for ^{58}Cu. (Left) The relative intensity plotted against the spin, I_i of the peak. (Right) Relative intensity plotted against the excitation energy, keV.

5.3 ^{53}Fe

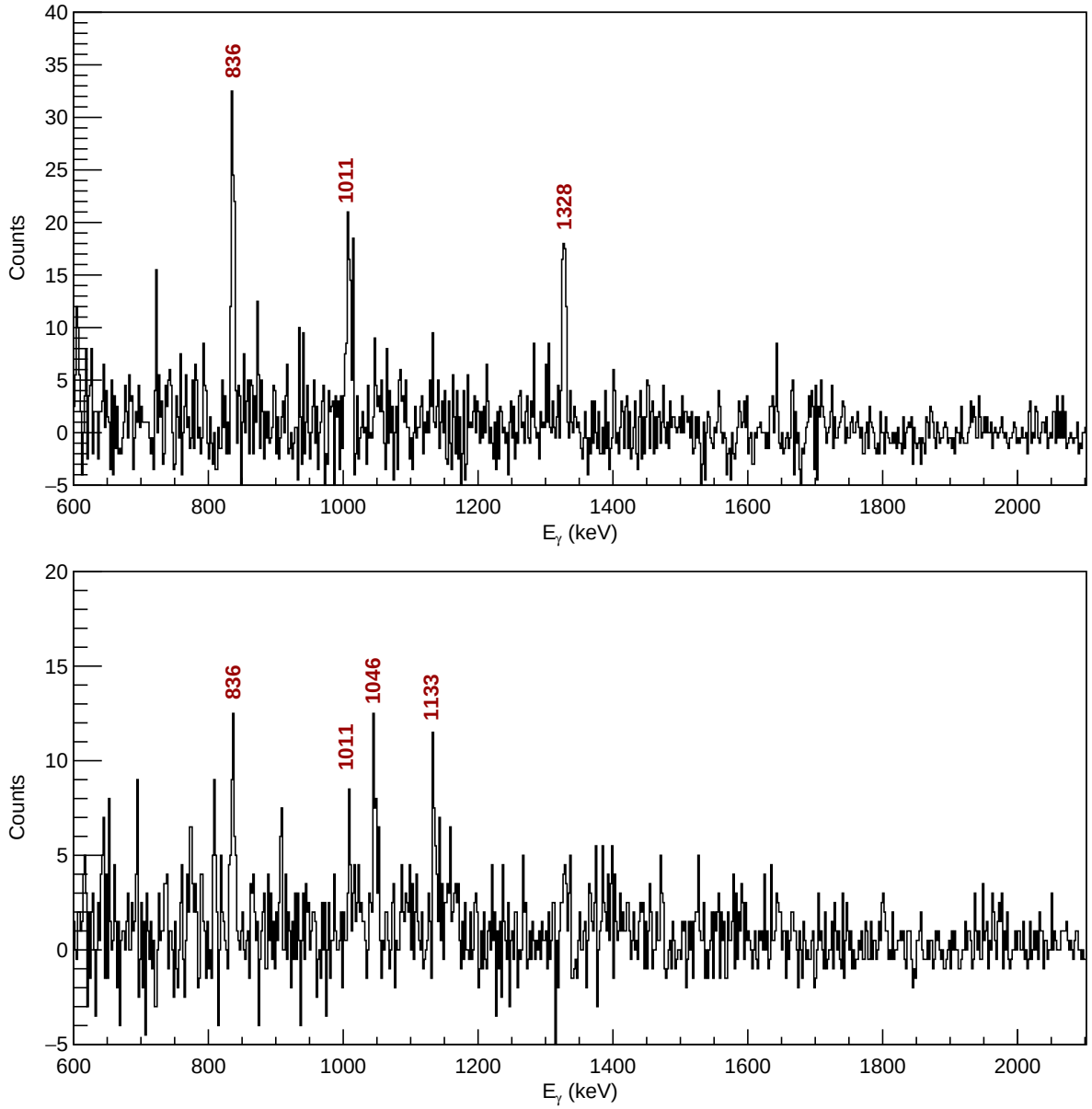

Figure 18: The graphs contain the γ-ray coincidence spectra for the two evaporation channels of ^{53}Fe produced from gating on the 124-keV transition. (Top) The 2pn spectrum corresponding to the 2pn evaporation channel. (Bottom) The dp spectrum. The red text indicates identified transitions that are labelled with their energies in keV.

The γ-γ matrix created from filtering for charged evaporates did not allow gating upon any of the desired transitions of ^{53}Fe. This was due to the coincident transitions of interest having low statistics comparative to the overall background. Gating was possible for the 2pn and dp matrix. However, the statistics are small with only three visible transitions. The resulting coincidence spectra are displayed in Figure 18. The peaks at 1046-keV and 1133-keV are from ^{60}Cu. These are highlighted in the decay scheme for ^{53}Fe [17] displayed in Figure 19. The intensities from ^{53}Fe are tabulated in Table 5.

The relative intensities of transitions in the dp spectrum to the 2pn spectrum were plotted against spin and excitation energy is displayed in Figure 20. No fit was applied due to a lack of data. It appears that there is a trend of increasing dp ratio coinciding with increasing spin and excitation

energy is observed. However, due to the lack of data points it is not possible to make any definite claim.

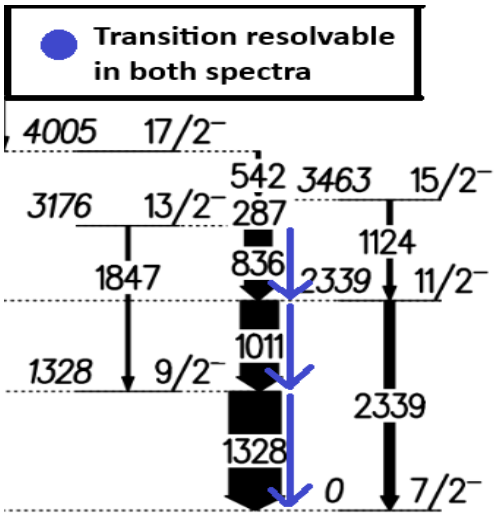

Figure 19: The relevant section of the decay scheme for ^{53}Fe adapted from [17]. The blue arrows indicate the transitions seen in the 2pn and dp spectrum.

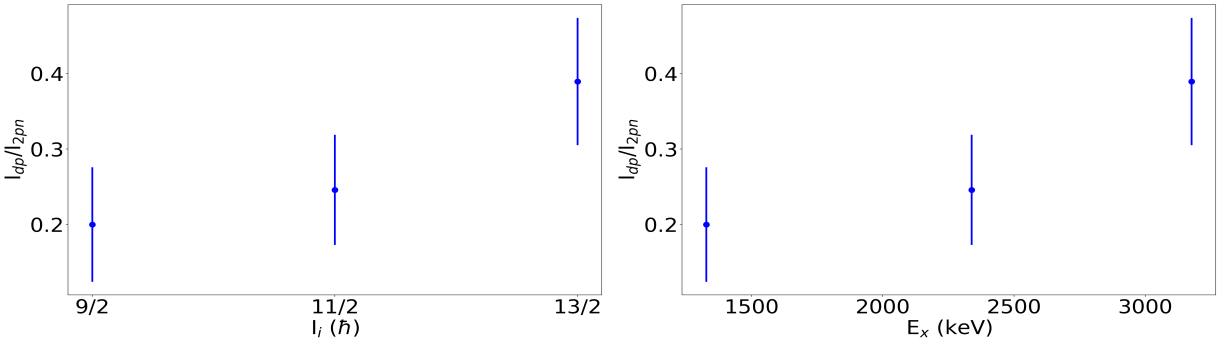

Figure 20: The relative intensities of peaks from the coincidence spectrum with dp settings to 2pn and spectrum for ^{53}Fe. The left is the ratio plotted against spin, I_i, of the state and right the against excitation energy, keV.

5.4 ^{49}Cr

Figure 21 displays the 2p and dp γ-ray coincidence spectra that are created by gating on the 272-keV ground-state transition in ^{49}Cr. The counts of the spectra reveal that the 2pn evaporation channel is the dominant decay channel of the pair. Using the 479-keV transition as a reference point is is clear that the 575-keV, 937-keV, 1177-keV, and 1628-keV peaks are relatively stronger in the dp spectrum. This indicates that the evaporation of a deuteron causes the recoil to populate different energy and spin states relative to the evaporation of a proton-neutron pair.

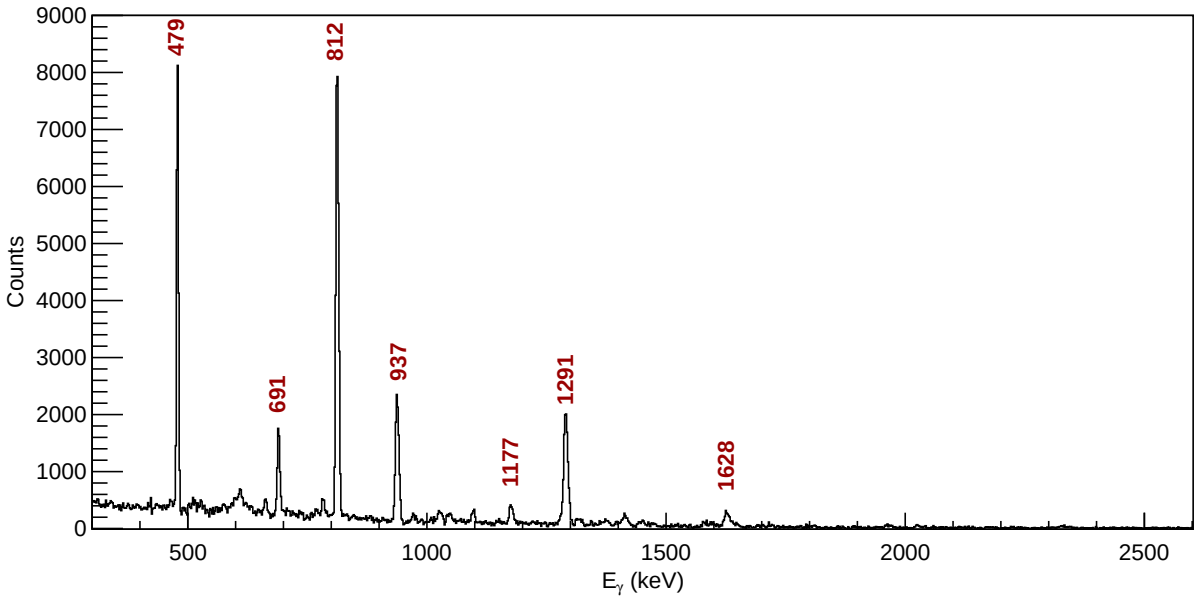

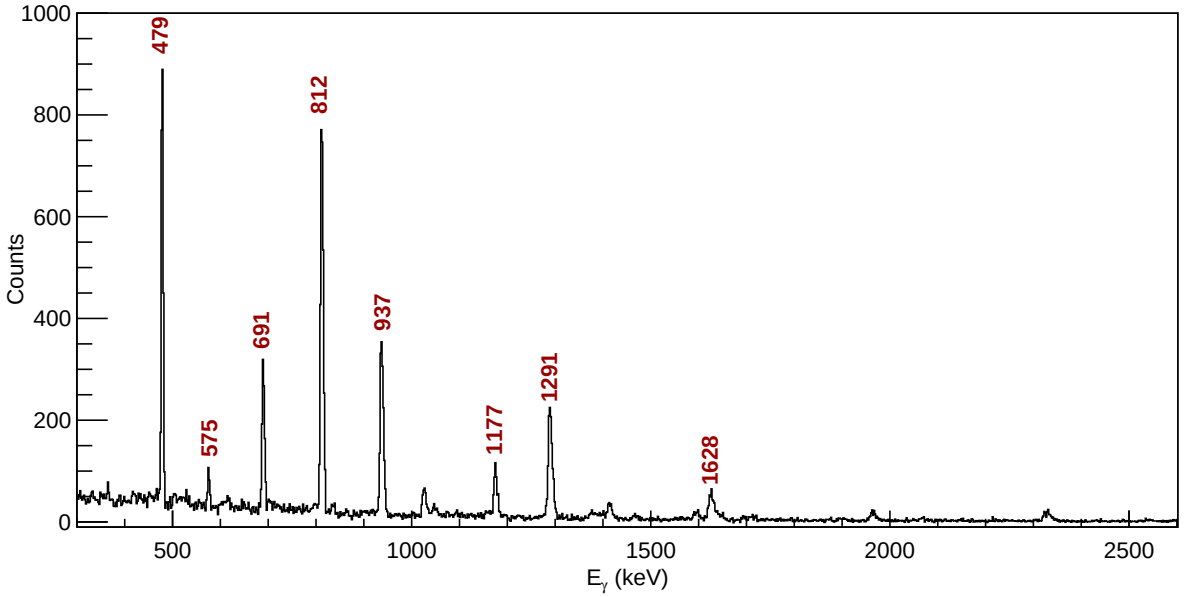

Figure 21: The graphs contain the γ-ray coincidence spectra for the two evaporation channels of ^{49}Cr produced from gating on the 124-keV transition. (Top) The 2p spectrum corresponding to the 2pn evaporation channel. (Bottom) The dp spectrum. The red text indicates identified transitions that are labelled with their energies in keV.

The transition of each resolvable peak for the 2p, 2pn, and dp spectra are tabulated in Table 6. The decay scheme for ^{49}Cr [18, 19, 20] is displayed in Figure 22. The later two references present a slightly more comprehensive decay scheme of ^{49}Cr. The right hand side of the decay schemes differ and needs to be studied in greater detail. The blue arrows indicate transitions seen in all three spectra. The yellow arrow indicates the transition only resolvable in the 2p spectrum and red arrows for transitions only resolvable in the dp spectrum. The 1396-keV transition is not present in the 2pn or dp spectrum with relatively low yield in the 2p spectrum. Therefore, the absence of this peak in the dp and 2pn spectra is a result of these spectra containing a lower quantity of statistics. The 1597-keV transition could not be resolved in the 2p spectrum due to background interference in the energy region. The four energy transitions in red are exclusively seen in the dp spectrum. The 364-keV, 836-keV, and 2070-keV transitions originate from the right decay branch. The last is the 148-keV transition from the left branch. The absence of these peaks from the 2p

spectrum, which, contains approximately five times the statistics, strongly indicates that the dp evaporation channel has a proclivity to populate higher excitation energy and spin stated.

The relative intensity of peaks from the dp to the 2p and 2pn spectra are plotted against spin and excitation energy in Figure 23. The 2332-keV transition was omitted due to large uncertainty. The relative intensity of the dp to the 2pn spectrum omitted use of the 575-keV transition due to the 2pn peak having a large uncertainty in intensity. It is clear that the ratio increases with respect to excitation energy and spin. The red line and shaded region display the linear fit and uncertainty region. The fit appears to decently capture the majority of data points and represents the overall trend. The fitting parameters are contained in Table 7. Figure 24 plots the relative intensity of the peaks in the 2pn spectrum against peaks from the 2p spectrum. A horizontal line is expected and seems to be achieved with the fit.

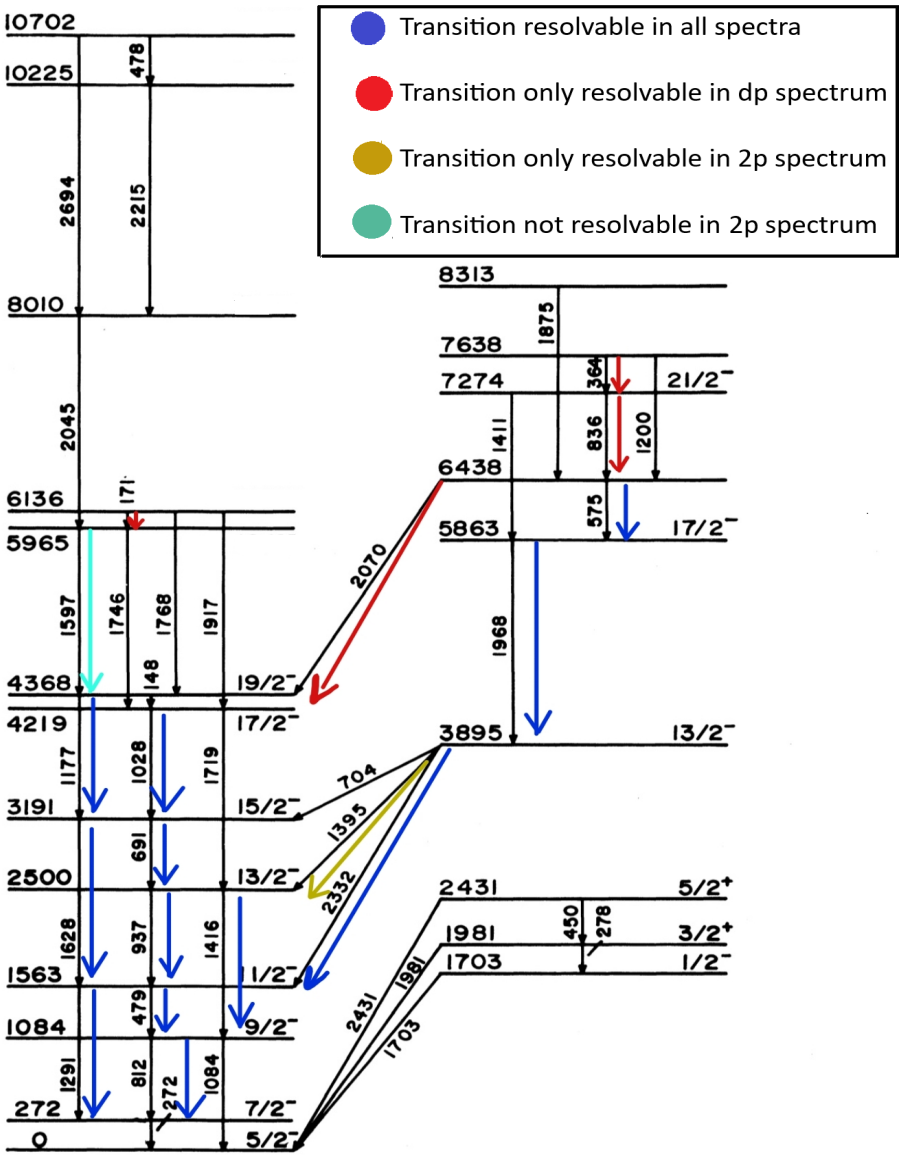

Figure 22: The decay scheme for ^{49}Cr adapted from [18]. The blue arrows indicate transitions resolvable in all spectra. The red arrows are transitions only resolvable in the dp spectrum. The yellow arrows for the transition only resolvable in the 2p spectrum. The light blue arrow for the transition not resolvable in the 2p spectrum.

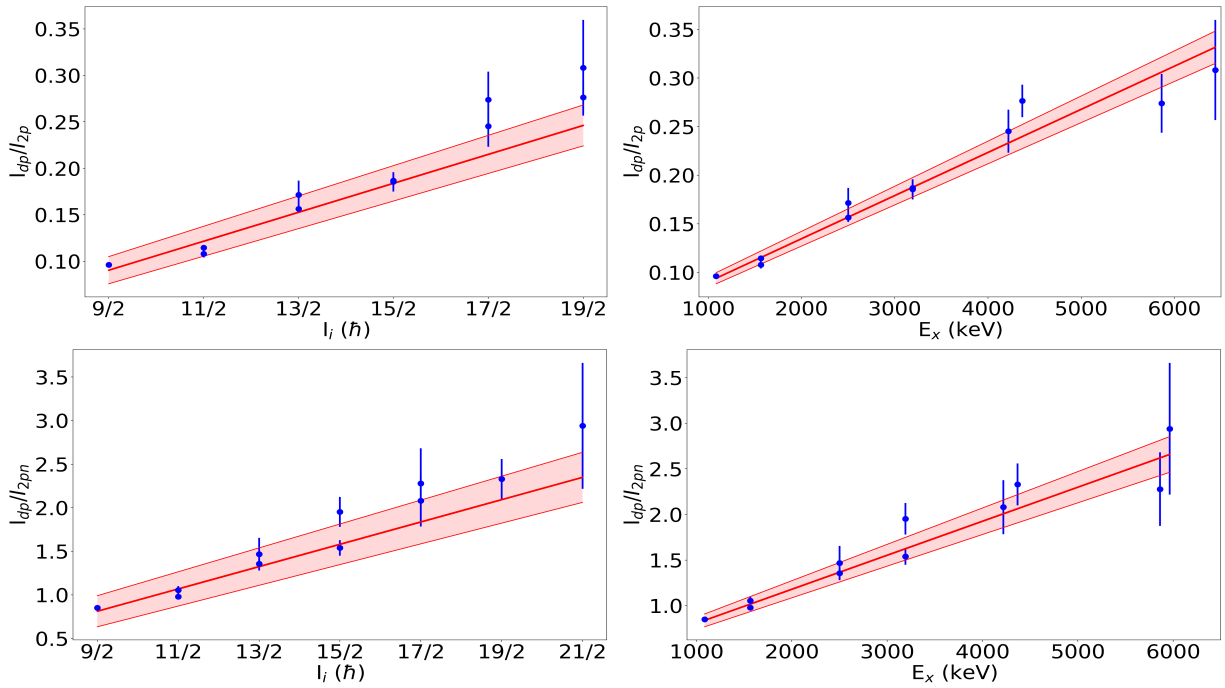

Figure 23: The relative intensities of peaks in the coincidence spectrum with dp settings against the 2p and 2pn spectra for ^{49}Cr. The top row is for 2p and the bottom 2pn. The left is the ratio plotted against spin, I_i, and the right against excitation energy, keV.

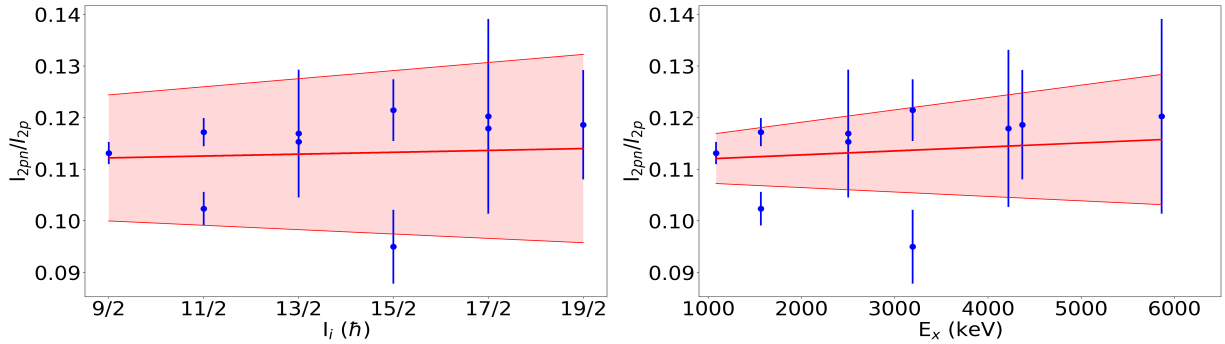

Figure 24: The relative intensities of peaks from the coincidence spectrum with 2pn settings against 2p spectrum for ^{61}Zn. (Left) The relative intensity plotted against the spin, I_i of the peak. (Right) Relative intensity plotted against the excitation energy, keV.

5.5 Relative intensity and mass number

To compare the relationship between the mass number of the recoil and the relative rate of decay from the dp evaporation channel with respect to the 2pn channel, an average was taken of the relative intensities calculated for ^{61}Zn, ^{53}Fe, and ^{49}Cr. The values are tabulated in Table 1. ^{61}Zn and ^{49}Cr contained many data points, therefore, the average was easily determined. ^{53}Fe only contained three data points that combined for a relatively low average ratio of 0.28(4). If one assumes that the rate of background intensity measured should be approximately constant then a background normalization factor should approximate this average. However, for the coincidence spectra produced for ^{53}Fe, displayed in Figure 18, this is clearly not the case. Looking at ^{61}Zn and ^{49}Cr it is clear that the ratio of peaks from the coincidence spectrum with dp settings to the ratio of the peaks with 2pn settings differ significantly, while the value for ^{53}Fe has a rather large uncertainty.

The same process was performed for the αd, αp, and αpn spectra for ^{58}Cu and the values are tabulated in Table 2. Direct comparison cannot be made with the dp or 2pn decay channel due to the different detection efficiencies of an α particle compared to a proton. However, it is still of interest that the relative rate of deuteron evaporation to a proton-neutron pair in ^{58}Cu is significantly higher than for ^{61}Zn, this may again indicate that lower mass recoils results in a relatively higher probability of deuteron evaporation or it may suggest that recoils on the $N = Z$ line having a relatively higher chance of being formed from deuteron evaporation relative to the $N = Z+1$ line.

The efficiency of neutron detection can be approximated by taking the average ratio of the peak intensities from the 2pn spectrum relative to the 2p spectrum. This is tabulated in Table 1. The ratio could not be computed for ^{53}Fe as discussed in Section 5.3. The average is larger for ^{49}Cr than for ^{61}Zn. This likely results from the differing mass of the respective recoils resulting in the kinematics changing for the evaporates resulting in differing neutron detection efficiency.

The analogous average was taken for ^{58}Cu and is contained in Table 2. The value is in-between the analogous value for ^{61}Zn and ^{49}Cr. However, this is not conclusive as one would need to correct for the differing detection efficiencies for α particle detection compared to proton detection to make a direct comparison.

Table 1: The average relative intensity of the dp peaks to the 2p and 2pn peaks along with the average relative intensity of the 2pn peaks to 2p peaks.

Element	$< \frac{I_{dp}}{I_{2p}} >$	$< \frac{I_{dp}}{I_{2pn}} >$	$< \frac{I_{2pn}}{I_{2p}} >$
^{61}Zn	0.0204(9)	0.257(12)	0.0790(18)
^{53}Fe	—	0.28(4)	—
^{49}Cr	0.193(6)	1.71(9)	0.108(4)

Table 2: The average relative intensity for αd against αp and αpn along with the average relative intensity of αpn against αp.

Element	$< \frac{I_{\alpha d}}{I_{\alpha p}} >$	$< \frac{I_{\alpha d}}{I_{\alpha pn}} >$	$< \frac{I_{\alpha pn}}{I_{\alpha p}} >$
^{58}Cu	0.043(8)	0.40(9)	0.103(11)

6 Conclusion and Outlook

For a condensed summary of the paper, the CD-shaped DSSDs had sufficiently high energy granulation to discriminate evaporated protons and deuterons originating from a fusion-evaporation reactions. ^{61}Zn, ^{58}Cu, ^{53}Fe, and ^{49}Cr are the four recoils of interest in this study. Gamma-ray coincidence spectra were produced from projections upon γ-γ coincidence matrices which were sorted by coincident charged evaporate detection or coincident charged and neutral evaporate detection. The relationship between the rate of deuteron evaporation compared to a proton-neutron pair against spin and excitation energy was examined. Analysis led to the following four results.

- For the 2pn and dp evaporation channels resulting in ^{61}Zn and ^{49}Cr it appears that the evaporation of a deuteron causes the recoil to populate higher spin and excitation states relative to the evaporation of a proton-neutron pair.
- It appears that the evaporation of a deuteron becomes more likely as mass number decreases for nuclei along the $N = Z + 1$ line.

- It appears that deuteron evaporation is more favourable from ^{58}Cu than ^{61}Zn. This possibly indicates that deuteron evaporation is more favourable for nuclei on the $N = Z$ line compared with nuclei on the $N = Z + 1$ line.
- Four high spin and excitation energy states were seen in the coincidence spectrum created from deuteron proton evaporation that were not seen in the coincidence spectra created from the evaporation of two protons and a neutron for ^{49}Cr.

In this paper a linear relationship was investigated for the relative intensity of peaks in the dp spectra to peaks in the 2pn spectra against spin and excitation energy for the transitions. The approximation appeared to decently describe the trend. However, further study into the relationship is required. Investigation of further recoils created from the dp or 2pn evaporation channel would allow for further insights on the effects deuteron evaporation has on how the recoil populates spin and excitation energy states.

The method used for determining the overall relative rate of deuteron evaporation to a proton-neutron pair was by averaging the relative intensity of the resolvable peaks in the coincidence spectrum. A more sophisticated method such as normalizing the background of the dp spectrum to the 2pn spectrum will likely give more accurate results. Along with analysis of more residual nuclei on the $N = Z + 1$ line. The low statistics in ^{53}Fe meant only two nuclei on the $N = Z + 1$ could be investigated for the mass dependence.

Analysis and correction of the efficiencies for deuteron detection compared to proton detection in the DSSD detectors will allow for direct comparison between a dp and 2p coincidence spectrum along with determining the relative cross section of deuteron evaporation compared to a proton-neutron pair.

Neutron detection was investigated by into averaging peak intensities from the 2pn spectrum relative to the 2p spectrum for ^{61}Zn and ^{49}Cr. It appears that the neutron detection efficiency varies between these two recoil. A further investigation into if this is a result of differing kinematics should be performed. Correcting for the differing neutron detection efficiency would also allow for direct comparison between analysis that uses a 2p spectrum and one that uses a 2pn spectrum.

To expand the study, other evaporation channels should be studied such that the recoils are on the $N = Z$ line and for other recoils further from the $N = Z$ line to determine if this is a factor on the rate of deuteron evaporation. The only $N = Z$ recoil studied in this paper was ^{58}Cu which appeared to show deuteron evaporation had a small or no relationship to spin or excitation energy. However, ^{58}Cu appeared to relatively favour deuteron evaporation over ^{61}Zn. Both of these nuclei originate from ^{64}Ge*. For a direct comparison between the different evaporation channels, detection efficiencies for α particle detection relative to proton detection should be determined.

The results for ^{49}Cr may change depending on which decay scheme one uses for ^{49}Cr. It may be possible to use the present data set to study the decay scheme of ^{49}Cr in further detail, which may resolve discrepancies in the right side of the decay branch.

Finally, a further investigation to the most interesting result of the paper which was the presence of four transitions in the dp spectrum for ^{49}Cr that were not seen in the 2p spectrum despite the 2p spectrum having considerably more statistics. The higher energy states may be explained by the 2.2-MeV binding energy of the deuteron. Possibly studying further lower mass recoils, which, may have larger rates of deuteron formation will allow for further investigation to how a recoil populates energy and spin states if a deuteron was evaporated compared to a proton-neutron pair.

7 References

[1] Argonne National Laboratory Official Website. https://www.anl.gov/. Accessed: 2024-05-07.

[2] Rudolph. D et al. *Particle and γ-Ray Coincidence Spectroscopy of ^{57}Cu.* ANL Proposal.

[3] Sarantites. D. G, et al. *"The microball" Design, instrumentation and response characteris- tics of a 4π-multidetector exit channel-selection device for spectroscopic and reaction mechanism studies with Gammasphere.* Nuclear Instruments and Methods in Physics Research Section A: Accelerators, Spectrometers, Detectors and Associated Equipment, 381(2):418–432, 1996.

[4] Kulenkampff. J, et al. *Geoscientific process monitoring with positron emission tomography (geopet).* Solid Earth, 7:1217–1231, Aug 2016.

[5] Lilley. J. *Nuclear Physics: Principles and Applications* . Manchester Physics Series. Wiley, 2013.

[6] Sarantites D. G, et al. *"Neu- tron Shell": A high efficiency array of neutron detectors for γ-ray spectroscopic studies with Gammasphere.* Nuclear Instruments and Methods in Physics Research Section A: Accelerators, Spectrometers, Detectors and Associated Equipment, 530(3):473–492, 2004.

[7] Argonne National Laboratory Official Website: Gammasphere. https://www.anl.gov/phy/gammasphere. Accessed: 2024-05-07.

[8] Argonne National Laboratory Official Website: Fragment Mass Analyzer. https://www.anl.gov/phy/fragment-mass-analyzer. Accessed: 2024-05-07.

[9] Lee. I-Y. *The Gammasphere.* Nuclear Structure in the Nineties. Nuclear Physics A, 520:c641–c655, 1990.

[10] Farghaly. D. *Nuclear Structure near the Proton Drip-line: A Search for Excited States in ^{62}Ge.* http://lup.lub.lu.se/student-papers/record/9117612, 2022.

[11] Persson. M. B. L. *Digitised charged-particle discrimination in CsI detector signals.* http://lup.lub.lu.se/student-papers/record/9086774, 2022.

[12] Hrabar. Y. *Decay Modes Of Exotic Nuclei.* PhD thesis, Lund University, 2024, to be published.

[13] ROOT Official Website. https://root.cern/. Accessed: 2024-05-07.

[14] GitHub: hdtv. https://github.com/janmayer/hdtv. Accessed: 2024-05-07.

[15] Andersson. L-L. *A Trilogy of Mass A=61 : Superdeformed Structures, Exotic Decay, and Isospin Symmetry.* . Doctoral thesis (compilation), 2008.

[16] Rudolph. D, et al. *High-spin shell-model states near ^{56}Ni.* European Physical Journal A. Hadrons and Nuclei, 4(2):115–145, 1999.

[17] du Rietz. R, et al. *Investigation of high-spin states in ^{53}Fe.* Phys. Rev. C, 72:014307, Jul 2005.

[18] Cameron. J. A, et al. *High-spin gamma spectroscopy of recoil-separated ^{49}Cr, ^{49}V, and ^{46}Ti.* Phys. Rev. C, 44:1882–1891, Nov 1991.

[19] Brandlolini. F, et al. *Lifetimes in the middle of $1f_{7/2}$ shell: cross-conjugated nuclei ^{47}V and ^{49}C.* Nuclear Physics A, 693(3):517-532, 2001.

[20] Cameron. J. A, et al. *Spectroscopy of cross-conjugate nuclei ^{46}Ti-^{50}Cr and ^{47}V-^{49}Cr near the $f_{7/2}$-shell band termination.* Phys. Rev. C, 58:808–820, Aug 1998.

8 Appendix

Table 3: Excitation energy, transition energy, and yield of each resolvable peak in the 2p, 2pn, and dp coincidence spectra for ^{61}Zn.

		^{61}Zn 2p		^{61}Zn 2pn		^{61}Zn dp	
E_x (keV)	I_i ($\hbar$)	E_γ (keV)	Yield	E_γ (keV)	Yield	E_γ (keV)	Yield
8879	23/2	1595.8	200(40)	—	—	—	—
7295	23/2	1742.7	1750(60)	1742.4	122(15)	1741.4	49(8)
7284	21/2	2637.6	460(40)	2637.3	43(9)	2639.6	15(5)
7284	21/2	1732.3	1330(50)	1732.3	122(14)	1731.2	44(7)
6212	21/2	1796.8	300(40)	—	—	—	—
6090	21/2	1674.1	5790(90)	1674.0	475(25)	1673.8	120(12)
5552	19/2	1288.4	3920(90)	1287.7	290(24)	1289.7	99(12)
5543	19/2	1700.5	2110(70)	1700.2	171(18)	1700.4	54(9)
5468	19/2	1623.7	470(40)	1619.3	32(12)	1623.1	24(6)
5254	19/2	993.2	1470(80)	993.0	140(22)	991.5	45(11)
5254	17/2	838.4	1530(70)	838.5	101(19)	—	—
4915	17/2	2116.8	840(50)	2118.5	85(13)	—	—
4644	17/2	1847.7	3620(80)	1847.0	264(20)	1856.8	72(10)
4415	17/2	1078.9	10380(120)	1078.5	790(34)	1078.6	230(17)
4264	15/2	1465.4	7050(110)	1465.8	576(29)	1466.6	182(15)
4264	15/2	1019.0	1390(70)	1017.7	119(20)	1019.8	19(9)
3844	15/2	1572.6	4130(80)	1572.1	296(22)	1573.1	67(10)
3844	15/2	1045.9	1590(80)	1045.9	99(20)	—	—
3495	15/2	2227.4	440(40)	2228.1	69(11)	—	—
3461	13/2	2196.6	1570(60)	2195.8	133(15)	2197.3	25(7)
3336	13/2	1065.5	1820(70)	1066.1	172(19)	1066.1	30(8)
3336	13/2	936.5	11510(140)	936.0	980(40)	936.2	194(17)
3244	11/2	1979.5	2010(60)	1980.2	162(16)	1979.8	39(7)
2799	13/2	1532.5	18480(150)	1532.6	1340(40)	1532.7	280(18)
2699	11/2	1434.3	2880(80)	1434.8	195(20)	1432.5	58(9)
2400	9/2	2274.8	530(40)	2271.9	71(12)	—	-
2400	9/2	1402.5	12750(130)	1402.4	969(35)	1401.4	243(17)
2270	11/2	1274.3	9080(110)	1274.6	634(30)	1273.6	143(14)
2270	11/2	1005.4	5630(100)	1005.7	406(26)	1005.8	61(11)
1266	9/2	1141.1	38370(210)	1141.0	2530(50)	1140.9	465(23)
998	7/2	872.7	32170(200)	872.6	2350(50)	872.8	444(23)

Table 4: Excitation energy, transition energy, and yield of each resolvable peak in the αp, αpn, and αd coincidence spectra for ^{58}Cu.

		^{58}Cu αp		^{58}Cu αpn		^{58}Cu αd	
E_x (keV)	I_i ($\hbar$)	E_γ (keV)	Yield	E_γ (keV)	Yield	E_γ (keV)	Yield
5347	9	1924.5	68(9)	1926.9	7.2(2.7)	1922	1.6(2.6)
5347	9	—-	—	906.0	8(4)	904.8	3.7(3)
4440	8	1020.9	130(13)	1021.1	15(4)	1018.6	5.9(3.1)
3420	7	1358.5	385(20)	1355.8	33(6)	1355.7	13(5)
3420	7	504.0	140(14)	504.9	8(4)	506.3	8(4)
2920	5	2478.9	139(14)	2480	15(5)	2476.6	9(3.3)
2064	5	516.9	393(22)	516.2	39(7)	512.0	11(5)
2064	5	1623.3	527(23)	1622.1	32(6)	1617.0	1.6(2.6)
1549	4	1106.5	660(27)	1105.3	75(9)	1105.6	27(6)

Table 5: Excitation energy, transition energy, and yield of each resolvable peak in the 2p, 2pn, and dp coincidence spectra for ^{53}Fe

		^{53}Fe 2p		^{53}Fe 2pn		^{53}Fe dp	
E_x (keV)	I_i ($\hbar$)	E_γ (keV)	Yield	E_γ (keV)	Yield	E_γ (keV)	Yield
1328	9/2	—	—	1327.1(4)	70(9)	1328.9(1.5)	14(5)
2339	11/2	—	—	1008.6(3)	61(8)	1009.3(5)	15(4)
3176	13/2	—	—	836.8(3)	95(10)	836.6(6)	37(7)

Table 6: Excitation energy, transition energy, and yield of each resolvable peak in the 2p, 2pn, and dp coincidence spectra for ^{49}Cr.

		^{49}Cr 2p		^{49}Cr 2pn		^{49}Cr dp	
E_x (keV)	I_i ($\hbar$)	E_γ (keV)	Yield	E_γ (keV)	Yield	E_γ (keV)	Yield
7638	23/2	—	—	—	—	364.7	58(18)
7274	21/2	—-	—	—	—	835.5	44(14)
6438	19/2	575.5	490(50)	573.0	26(15)	575.6	151(20)
6438	19/2	—	—	—	—	2067.1	38(7)
5965	21/2	—	—	1594.2	33(7)	1594.6	97(12)
5863	17/2	1965.2	449(23)	1965.1	54(8)	1965.1	123(12)
4368	19/2	1176.7	1610(50)	1176.2	191(16)	1175.8	445(23)
4368	19/2	—	—	—	—	149.5	90(20)
4219	17/2	1026.7	1060(50)	1026.1	125(15)	1027.4	260(20)
3895	13/2	1396.4	155(23)	—	—	—	—
3895	13/2	2334.1	555(25)	2327.9	38(7)	2331.2	179(14)
3895	13/2	—	—	—	—	703	71(16)
3191	15/2	1629.4	2200(50)	1628.5	209(15)	1628.8	408(21)
3191	15/2	690.1	5030(90)	690.0	611(28)	689.8	940(34)
2500	13/2	1413.4	1300(50)	1414.1	152(15)	1412.6	223(18)
2500	13/2	937.9	9590(110)	937.9	1106(35)	937.7	1500(40)
1563	11/2	1290.3	11030(110)	1290.3	1129(34)	1290.2	1190(40)
1563	11/2	478.6	19540(150)	478.4	2290(50)	478.4	2240(50)
1084	9/2	812.7	29520(180)	812.5	3340(60)	812.5	2840(60)

Table 7: The table contains the parameters for the linear fits applied to the ratios of intensity against spin and excitation energy in Section 5.1, 5.2, and 5.4.

		Spin		Excitation energy	
Element	Ratio	Gradient ($\hbar^{-1}$)	y intercept	Gradient (keV^{-1})	y intercept
^{61}Zn	I_{dp}/I_{2p}	$1.6(1)\cdot10^{-3}$	$6.7(2)\cdot10^{-4}$	$2.4(2)\cdot10^{-6}$	$1.0(1)\cdot10^{-2}$
^{61}Zn	I_{dp}/I_{2pn}	$1.6(3)\cdot10^{-2}$	$1.3(2)\cdot10^{-1}$	$2.3(4)\cdot10^{-5}$	$1.6(1)\cdot10^{-1}$
^{61}Zn	I_{2pn}/I_{2p}	$1.6(4)\cdot10^{-3}$	$6.4(2)\cdot10^{-2}$	$2.5(5)\cdot10^{-6}$	$6.7(2)\cdot10^{-2}$
^{58}Cu	$I_{\alpha d}/I_{\alpha p}$	$5(4)\cdot10^{-3}$	$3(20)\cdot10^{-3}$	$1.0(6)\cdot10^{-6}$	$9(50)\cdot10^{-3}$
^{58}Cu	$I_{\alpha d}/I_{\alpha pn}$	$3(6)\cdot10^{-2}$	$2(2)\cdot10^{-1}$	$5(6)\cdot10^{-5}$	$2(2)\cdot10^{-1}$
^{58}Cu	$I_{\alpha pn}/I_{\alpha p}$	$2(6)\cdot10^{-3}$	$8(3)\cdot10^{-2}$	$6(8)\cdot10^{-6}$	$8(2)\cdot10^{-2}$
^{49}Cr	I_{dp}/I_{2pn}	$3.1(1)\cdot10^{-2}$	$-5.0(8)\cdot10^{-2}$	$4.4(2)\cdot10^{-5}$	$4.6(4)\cdot10^{-2}$
^{49}Cr	I_{dp}/I_{2p}	$2.6(2)\cdot10^{-1}$	$-3(1)\cdot10^{-1}$	$3.7(3)\cdot10^{-4}$	$4.3(4)\cdot10^{-1}$
^{49}Cr	I_{2pn}/I_{2p}	$3(10)\cdot10^{-4}$	$1.1(0)\cdot10^{-1}$	$8(20)\cdot10^{-7}$	$1.1(0)\cdot10^{-1}$

Table 8: The energy gatings used for projections of desired transitions for the different recoils along with the energy gatings and normalization factors used for projections of background selections on the γ-γ matrix.

Recoil	Peak (keV)	Background 1 (keV)	Normalization	Background 2 (keV)	Normalization
^{61}Zn	[120-126]	[112-118]	0.5	[128-134]	0.5
^{58}Cu	[440-448]	[436-438]	1.0	[448-452]	1.0
^{53}Fe	[286-290]	[282-286]	0.5	[290-294]	0.5
^{49}Cr	[270-274]	[264-268]	0.5	[278-282]	0.5